Available online at www.sciencedirect.com

ScienceDirect

Geochimica et Cosmochimica Acta 319 (2022) 220–253

Geochimica et Cosmochimica Acta

www.elsevier.com/locate/gca

Characterization of hydrothermal fluids that alter the upper oceanic crust to spilite and epidosite: Fluid inclusion evidence from the Semail (Oman) and Troodos (Cyprus) ophiolites

Lisa Richter *, Larryn W. Diamond

Institute of Geological Sciences, University of Bern, Baltzerstrasse 3, CH-3012 Bern, Switzerland

Received 10 January 2021; accepted in revised form 9 November 2021; Available online 15 November 2021

Abstract

Pervasive alteration of basaltic oceanic crust by heated seawater at greenschist facies conditions produces two contrasting hydrothermal rocks. "Spilites", consisting of chlorite + albite + quartz ± actinolite ± epidote, occur typically with regional extents. Locally spilites are metasomatically transformed to "epidosites" consisting of epidote + quartz + titanite + hematite or magnetite. Both alteration types have been proposed as markers of deep hydrothermal upflow in sub-seafloor convection cells, and as sources of the ore metals in basalt-hosted seafloor massive sulfide deposits. Little direct evidence is available for the chemical compositions of these fluids in their states deep in the upflow zones prior to their discharge at the seafloor. To better characterize them we have conducted a field, petrographic and fluid inclusion study of the lavas, sheeted dikes and plagiogranites in the Semail ophiolite, with supporting samples from the Troodos ophiolite. Our results show that both the spilite- and epidosite-forming fluids were single-phase aqueous liquids during the hydrothermal alteration. At some sites their salinity is 3.1–3.2 wt.% $NaCl_{eq}$, which we take to represent the chlorinity of Cenomanian seawater in the Semail realm. At other sites salinities are as low as 2.4 wt.% $NaCl_{eq}$ or as high as 5.7 wt.% $NaCl_{eq}$, attributable to liquid–vapor separation and partial remixing deep in the crust along the dew curve of seawater, prior to ascent of the fluids to the sites of fluid inclusion trapping. Hypersaline brines, often accompanied by vapor, are restricted to plagiogranites in both the Semail and Troodos ophiolites and they represent magmatic–hydrothermal fluids that pre-date and are genetically unrelated to the spilite and epidosite alteration. The volcanostratigraphic locations of the samples constrain their maximum depths to 1470–3600 m below seafloor during alteration. The range of possible fluid trapping pressures for all samples is 31–68 MPa. Trapping temperatures vary between sites from 145 to 440 °C for spilite fluids and 255 to 435 °C for epidosite fluids. Quantitative analyses of 12 elements in individual fluid inclusions by LA-ICP-MS define the chemical characters of the two alteration fluids. The Br/Cl ratio in the spilite fluid is the same as in modern seawater and the other elements fit expectations from seawater–basalt experiments at elevated temperature. Accordingly, concentrations of Li, B, Na, Cl, K, Br and Sr in the spilite fluid match those in modern black-smoker vent fluids in basaltic crust. Exceptions are Ca and Fe, which are enriched in the spilite fluid. As these elements may precipitate below or at the seafloor prior to vent sampling, we conclude that the spilite fluids are plausible feeders of basalt-hosted black-smoker vents. The epidosite fluid has broadly similar elemental concentrations to the spilite fluid, but vastly lower Fe, reflecting the highly oxidized state of epidosites. This suggests that epidosite fluids are incapabable of forming basalt-hosted seafloor massive sulfide deposits.

Keywords: Spilite; Epidosite; Fluid inclusion; Hydrothermal alteration; Oceanic crust; Ophiolite; Massive sulfide; VMS

* Corresponding author.
E-mail address: lisa.richter@gmx.net (L. Richter).

https://doi.org/10.1016/j.gca.2021.11.012
0016-7037/

1. INTRODUCTION

Observations of in-situ oceanic crust, ophiolites and Archean greenstone belts show that vast quantities of basaltic lavas, dikes and intrusive rocks have been pervasively altered by deep circulation of magmatically heated seawater (Gillis and Banerjee, 2000; Hannington et al., 2003; Staudigel, 2014). The associated leaching and transport of elements, which ultimately influences ocean chemistry and forms volcanogenic massive sulphide (VMS) deposits, is mostly ascribed to regions of the crust that are hydrothermally altered at greenschist facies P–T conditions. There, the alteration mineralogy testifies to sufficiently high temperatures to raise mineral solubilities (~200–450 °C; German and Von Damm, 2006; Hannington, 2014), while the intensity and extent of alteration testifies to sufficiently high water–rock ratios to effect significant exchanges of mass.

Two contrasting types of alteration form under these P–T conditions. Volumetrically dominant is "spilite" alteration (Cann, 1969), by which the basalts are transformed to albite–chlorite–quartz ± epidote ± actinolite ± titanite ± hematite or magnetite, often preserving relict igneous clinopyroxene. The alteration enriches the rocks in Na and Mg and depletes them in Ca (along with other element transfers). This metasomatism is typical of the sheeted dike complexes in the in-situ oceanic crust, a subtype of the "background" or rock-matrix alteration described by Heft et al. (2008) and Alt et al. (2010). The second type of alteration involves pervasive transformation of pre-existing spilites into massive "epidosites". These consist essentially of epidote + quartz with minor titanite ± hematite or magnetite in their end-member state, although most epidosite bodies contain relict spilitic chlorite and igneous clinopyroxene (Richardson et al., 1987; Schiffman and Smith, 1988; Harper, 1995; Weber et al., 2021). The epidosite mineralogy reflects a reversal of the spilite metasomatism: Ca is enriched in the rock while Mg and Na are quantitatively depleted (along with other element transfers). Quartz–epidote veins are locally associated with massive epidosites. In the in-situ oceanic crust, quartz–epidote veins are widespread but massive replacement epidosites have been found only rarely (Quon and Ehlers, 1963; Vanko et al., 1992; Banerjee et al., 2000; Teagle et al., 2006). However, massive epidosites are common in basaltic lavas in Archean greenstone belts (Galley, 1993; Hannington et al., 2003) and in Phanerozoic ophiolites, where they occur within the sheeted dike complexes and the overlying lavas (Gillis and Banerjee, 2000; Gilgen et al., 2016).

Spilites and epidosite are thus present in a variety of tectonic settings and fluid flow regimes. In the in-situ oceanic crust, spilite alteration has been traditionally ascribed to water–rock interaction along deep downflow paths of hydrothermal circulation cells (e.g., Mottl, 1983), but formation during upflow has also been suggested (e.g., Coogan, 2008, Heft et al., 2008, Alt et al., 2010). Epidosite alteration is thought to occur in the deep upflow zones of circulation cells (Richardson et al., 1987; Schiffman and Smith, 1988; Galley, 1993; Weber et al., 2021). Both altered rock types have been proposed as sources of the metals in VMS deposits (Richardson et al., 1987; Alt et al., 2010; Jowitt et al., 2012; Patten et al., 2017).

The physicochemical properties of the fluid that causes spilite alteration are constrained by analyses of seafloor hydrothermal vent fluids. However, as vent fluids are typically modified by mineral precipitation and boiling at or near the seafloor, important features of the deep fluid remain poorly defined by direct observations, such as the concentrations of the key elements Mg and Fe. Much less is known about the properties of the fluid that causes epidosite alteration. Opinions vary regarding its phase state (i.e., whether a one-phase or a two-phase fluid system is involved) as well as its salinity and density (detailed below). Its major-element composition can be partly constrained by thermodynamic modelling, but such models require the basic fluid properties as input (e.g. Weber et al., 2021).

Beyond the current reach of fluid sampling at the seafloor, direct information on the properties of deep spilitizing and epidotizing fluids (also referred to hereafter simply as "spilite fluids" and "epidosite fluids") can be gained from fluid inclusion analyses, as demonstrated by numerous studies of in-situ crust and ophiolites (reviewed below). In the present study we verify published fluid inclusion evidence from the Semail and Troodos ophiolites by conducting new analyses from the same outcrops as those sampled in previous studies. Further, as the main contribution of this study, we expand the available data set by presenting analyses of fluid inclusions and their coeval mineral assemblages in new spilite and epidosite samples from the volcanic sequence of the Semail ophiolite. This allows us to reconstruct the phase states, salinities, densities and major element concentrations of the spilite and epidosite fluids, as well as the depth, fluid pressure and temperature at which the fluids were trapped as inclusions. Thus, the characterizations of fluids and mineral assemblages that we obtain correspond to well defined thermodynamic states that are independent of the tectonic setting in which the alteration occurs. Our results can therefore be used as calibration targets for future numerical simulations of reactive transport through oceanic crust in a variety of tectonic environments, ancient and modern.

2. GEOLOGICAL SETTING

2.1. Geology of the Semail and Troodos ophiolites

The Semail oceanic crust formed in the southeastern Tethys Ocean (Lippard et al. 1986; Searle and Cox, 1999) in just a 1 million year interval (96.1–95.2 Ma; Rioux et al., 2021) during the Cenomanian. Following its obduction the ophiolite was warped into a broad NW–SE-trending antiform (Fig. 1A), tilting the crustal layering such that erosion has now exposed oblique cross-sections in outcrop.

The lower crust is 0.5–4 km thick and is composed dominantly of layered gabbros capped by a continuous sheet of isotropic gabbros including sparse lenses and stocks of "plagiogranite" (i.e., members of the tonalite–trondhjemite–diorite suite; Fig. 1B). As the isotropic bodies

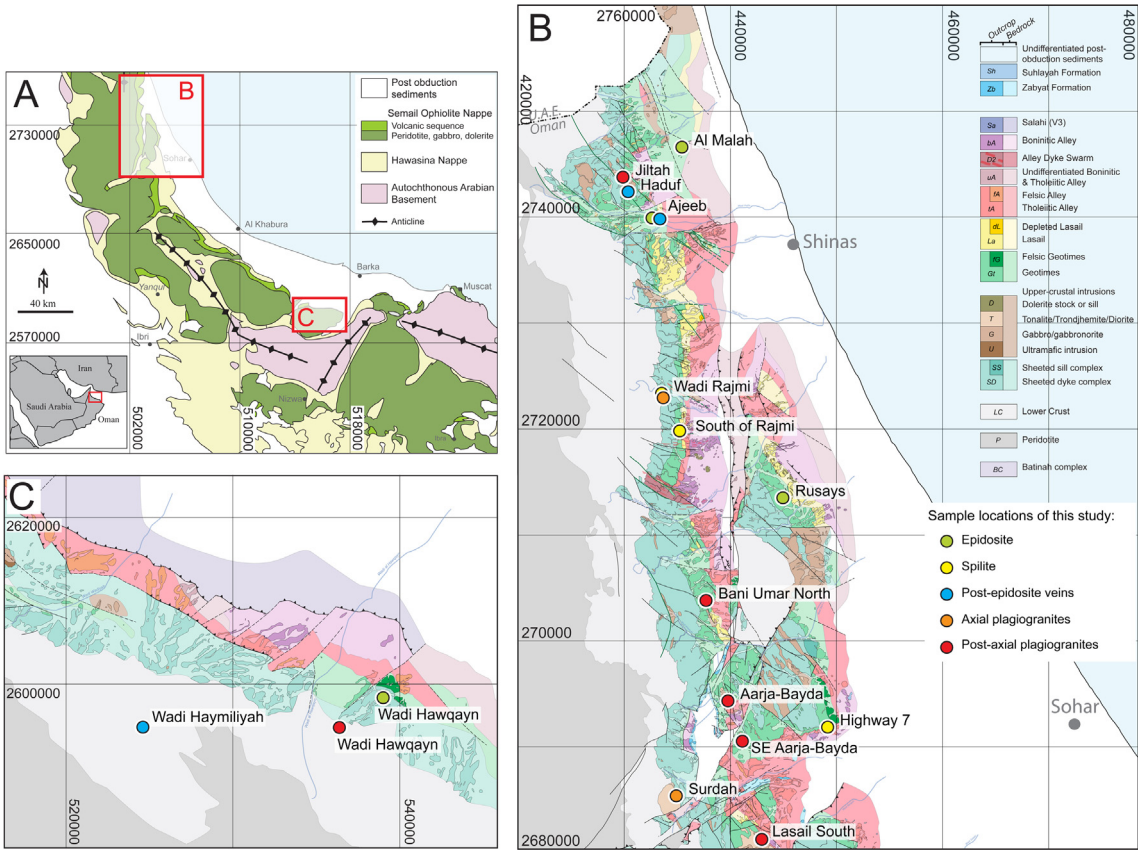

Fig. 1. Geological maps of the Semail ophiolite showing sample locations of this study: (A) Geological overview (modified after Gilgen et al., 2014); (B) North-eastern flank of the Semail ophiolite (modified after Belgrano et al., 2019) with locations of sampled plagiogranites, spilites, epidosites and post-epidosite veins. (C) Halayn block with locations of sampled plagiogranite, epidosite and post-epidosite veins (modified after Belgrano et al., 2019).

are the highest units in the lower crust, Lippard et al. (1986) termed them "High Level Intrusives". Haase et al. (2016) referred to them as the "Phase 1 (P1)" generation.

The base of the upper crust is a 1–1.5 km thick sheeted dike complex (SDC) with MORB-like major element composition (Fig. 2). This overlies the High Level Intrusives and grades upwards into comagmatic basalt to basaltic–andesite lavas (pillows, feeder dikes and rarer sheet flows) of the Geotimes unit (Alabaster et al., 1982). All of the rocks mentioned above are thought to have formed at a fast spreading axis along an oceanic ridge, which was situated from its outset above a nascent subduction zone (e.g., Pearce et al., 1981; Belgrano and Diamond, 2019, and references therein).

The axial Geotimes lavas transition upwards to primitive, mainly off-axis basaltic lavas of the Lasail unit, which are in turn overlain by up to 2 km of post-axis (Phase 2) pillow lavas, sheet flows, sills and feeder dikes of mostly basaltic to andesitic composition belonging to the Tholeiitic Alley and Boninitic Alley units (Alabaster et al., 1982; Belgrano et al., 2019). During Tholeiitic Alley volcanism, stocks of gabbro and plagiogranite intruded throughout the length of the ophiolite at all crustal levels, from the deep layered plutonic series through to the shallow Boninitic Alley lavas (Lippard et al., 1986; Belgrano et al., 2019). Owing to their timing, Lippard et al. (1986) termed these stocks "Late Intrusives", and Haase et al. (2016) referred to them as the "Phase 2 (P2)" generation. Herein we refer to the two generations of gabbros, plagiogranites and lavas in the ophiolite simply as "axial" and "post-axial".

Volcanogenic massive sulfide (VMS) deposits in the Semail ophiolite occur in all four volcanic units throughout the history of late axial to late post-axial volcanism. All the deposits are dominated by copper with only minor zinc, regardless of the host lava unit, but the deposits within Boninitic Alley are enriched in gold (Gilgen et al., 2014).

The oceanic crust in the Troodos ophiolite has a layered structure and an early axial-spreading origin similar to the Semail ophiolite (Gass, 1980). In Troodos, however, the axial gabbros, the overlying sheeted dike complex, the dike–lava transitional Basal Group and the overlying Lower Lavas all have arc-tholeiitic BADR compositions rather than MORB-like, owing to stronger influence from an underlying subduction zone (Robinson et al., 1983). The Upper Lavas in Troodos are boninitic (as in Semail) to high-Mg andesitic in composition (Pearce and Robinson, 2010). Whereas at least two major generations and stratigraphic settings of plagiogranite are present in

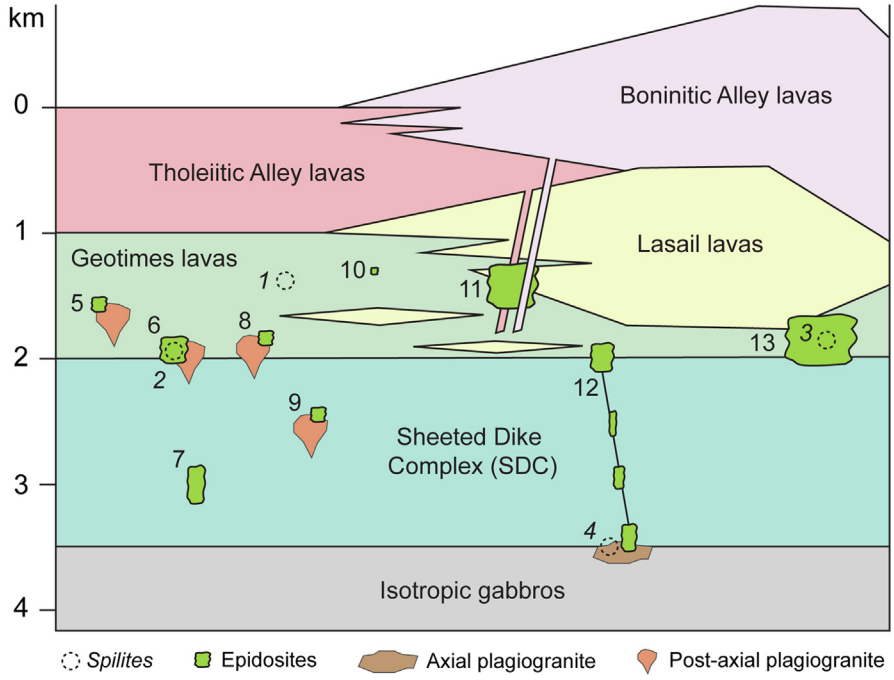

Fig. 2. Upper crustal stratigraphy of the Semail ophiolite based on Belgrano and Diamond (2019). SDC – Sheeted Dike Complex; Geotimes (axial), Lasail (off-axial), Tholeiitic Alley (post-axial) and Boninitic Alley (post-axial) – basaltic to basaltic-andesite lava units, mostly altered to spilite. Spilite and epidosite sample locations for this study: 1 – Highway 7, 2 – Bani Umar North, 3 – Rusays, 4 – Wadi Rajmi, 5 – Aarja-Bayda, 6 – Bani Umar North, 7 – Wadi Hawqayn, 8 – Jiltah, 9 – Wadi Hawqayn, 10 – Al Malah, 11 – Ajeeb, 12 Rajmi, 13 – Rusays. Numerous other known epidosites in the SDC, Geotimes and Lasail lavas (Gilgen et al., 2016) are not shown.

Semail, plagiogranites in Troodos occur only in the gabbros and in the sheeted dike complex but not in the lavas (e.g., Gass, 1980; Marien et al., 2019). Similarly to Semail, VMS deposits occur throughout the history of volcanism (Adamides, 2010).

2.2. Spilite alteration in the Semail and Troodos upper crust

The vast majority of sheeted dikes and lavas in the Semail ophiolite show pervasive hydrothermal alteration, dominantly to spilite. The SDC and the Geotimes and Lasail lavas all display greenschist-facies alteration (see Section 5.1 for details), with glass being extremely rare (Kusano et al., 2017; Belgrano et al., 2019). The Tholeiitic Alley and Boninitic Alley lavas also contain chlorite, albite and quartz even locally up to the top of the volcanic sequence, with smectite, prehnite and zeolites attesting to a lower grade overprint (Alabaster and Pearce, 1985; Pflumio, 1991; Belgrano et al., 2019). We focus the present study on the axial SDC and Geotimes lavas that exhibit greenschist-facies spilite alteration, including spilitized and epidotized plagiogranites of post-axial age that sit within these units. According to radiometric dating by Rioux et al. (2021), the axial magmatism occurred between 96.1 and 95.6 Ma and was followed without a significant pause by post-axial magmatism between 95.6 and 95.2 Ma. It is thus possible to view the large-scale hydrothermal alteration of the ophiolite as one extended regime through time.

Hydrothermal–metamorphic alteration in the Troodos ophiolite (Gillis and Robinson, 1990) shows a different vertical distribution compared to Semail. The lavas are limited to chlorite–smectite grade, with chlorite–albite–quartz spilites appearing in the upper SDC, and actinolite-bearing spilites appearing towards its base. In the Troodos literature spilitized dikes are referred to as "diabases" (e.g., Cann et al., 2015).

2.3. Epidosite alteration in the Semail and Troodos upper crust

In the Semail ophiolite, massive epidosites are occasionally present within the SDC with extents up to 0.15 km^2. Such epidosites were previously thought to be confined to the base of the SDC (Nehlig et al., 1994; Juteau et al., 2000) as in Troodos, but Gilgen et al. (2016) showed that essentially identical epidosites occur more frequently and with much larger outcrop extents (up to 1 km^2) in the overlying lava units. In all units the epidosites overprint precursor spilite alteration (Weber et al., 2021). All these epidosites are accompanied by sparse epidote–quartz veins. Numerous plagiogranite intrusions (both axial and post-axial) host patchy epidosite alteration (Nehlig et al., 1994; Gilgen et al., 2016). Nehlig (1991) suggested that each epidotized dyke in the SDC was altered individually soon after its intrusion, during active seafloor spreading. In contrast, Gilgen et al. (2016) showed from cross-cutting relations of dikes with known volcanostratigraphic affinity that most, and possibly all, epidosites in the Semail ophiolite formed after axial spreading had ceased. The epidosite alteration overprinted the upper crustal sequence and its enclosed

post-axis intrusions once the Lasail unit and some of the overlying Tholeiitic Alley and Boninitic Alley units had already erupted (Fig. 2).

In the Troodos ophiolite, massive epidosites occur abundantly within an area of ~10 km^2 as large, pervasive replacements of the SDC and the upper gabbros, and as patchy alteration of plagiogranites at the gabbro–SDC boundary (Richardson et al., 1987; Schiffman and Smith, 1988). Within these areas, the percentage of end-member epidosites is small (e.g., Jowitt et al., 2012). The alteration in the plagiogranites affects large volumes of rock but individual epidosite bodies within them are often only pods of a few dm^3 to cm^3 in volume. In contrast to Semail, epidosites in the Troodos volcanic sequence are extremely rare, despite ample outcrops. A paleomagnetic study by Varga et al. (1999) suggested the epidosites formed prior to cessation of the seafloor spreading that created the SDC. Based on cross-cutting relations of dikes with striped epidosite alteration, Cann et al. (2015) argued that each individual dike had been epidotized immediately upon its intrusion, before the next adjacent dike intruded the SDC, as suggested by Nehlig (1991) for Semail. However, Gilgen et al. (2016, p. 207) pointed out that the same cross-cutting relations in Troodos can be alternatively explained by a single influx of epidotizing fluid after large segments of the heterogeneously permeable SDC had already formed.

3. PREVIOUS FLUID INCLUSION STUDIES OF OCEANIC SPILITES AND EPIDOSITES

3.1. Fluid inclusions in spilites

Previous fluid inclusion studies agree on the basic properties of the spilite fluid that has altered the SDC and SDC-lava transition in in-situ oceanic crust (Fig. 3A, field 1; e.g., Gallinatti, 1984; Delaney et al., 1987; Saccocia and Gillis, 1995; Heft et al., 2008; Alt et al., 2010; Castelain et al., 2014) and in the Troodos ophiolite (Kelley et al., 1992; Gillis, 2002). Quartz is the only host mineral that has yielded tractable inclusions, but even these are typically very small. Owing to petrographic limitations, few studies have been able to identify primary inclusions from the abundant secondary and other inclusions of equivocal age with respect to quartz. Only aqueous liquid-dominated liquid–vapor (LV) inclusions have been found, suggesting that only one liquid phase was present in the rocks during spilite alteration and fluid inclusion entrapment. The salinities of the inclusions vary from 0.1 to 10.1 wt.% $NaCl_{eq}$, straddling the salinity of modern seawater (3.0–3.8 $NaCl_{eq}$, or 3.1–3.9 TDS; Levitus et al., 1994). This variation is attributed to high temperature liquid–vapor separation of seawater and partial remixing at depth, prior to entrapment of the inclusions (discussed further in Section 6.3.2). Homogenization temperatures (T_h(LV→L)) vary over a broad, 320 degree range from 130 to 450 °C, implying that fluid was trapped over a similarly broad range of temperatures. Temperatures of entrapment (T_{trap}) are typically 10–40 °C higher than the measured T_h values, as estimated by adding a correction to T_h based on the hydrostatic pressure of cold seawater at the known or estimated depth of entrapment. Presumably the spilite alteration assemblage, involving chlorite, quartz, albite and often actinolite, formed in the upper half of the T_{trap} range.To our knowledge there is so far no record of hypersaline (halite-bearing) brines in the SDC or the overlying lavas from the in-situ or ophiolite crust. However, liquid–vapor–halite (LVH) inclusions with salinities of 31–61 wt.% $NaCl_{eq}$ and conjugate vapor-dominated LV inclusions with very low salinities (1–4 wt.% $NaCl_{eq}$) are abundant in plagiogranites, felsic dikes and some gabbros (Fig. 3A, field 4: Kelley et al., 1992; Vanko et al., 1988, Vanko et al., 1992; Kelley and Früh-Green, 2001; Alt et al., 2010; Castelain et al., 2014; Bali et al., 2020). Both primary and secondary inclusions occur in igneous quartz and apatite, and in quartz ± epidote veins. The common occurrence of hypersaline brine and vapor in felsic intrusives and not in nearby gabbros suggests that they are exsolved magmatic fluids rather than seawater that has undergone liquid–vapor separation (Kelley and Früh-Green, 2001). The plutonic rocks also contain abundant primary and secondary LV inclusions of the same spilite type as in the SDC and lavas (Vanko et al., 1988, Vanko et al., 1992; Nehlig, 1989, 1991; Alt et al., 2010; Castelain et al., 2014), with salinities of 0.5–9.2 wt.% $NaCl_{eq}$ and homogenization temperatures of 125 °C to over 500 °C (Fig. 3A, field 2). Less common are LV inclusions with salinities of 2–23 wt.% NaCl, which almost bridge the low-salinity LV and hypersaline fluid types (Fig. 3A, field 3; Kelley et al., 1992; Vanko et al., 1992; Castelain et al., 2014). These may be due to condensation and remixing of the magmatic fluids (Kelley and Früh-Green, 2001).

3.2. Fluid inclusions in epidosites

Previous fluid inclusion studies on epidosites are restricted almost exclusively to the Troodos and Semail ophiolites (Fig. 3B). Two contrasting types of fluids have been found associated with the epidosites and deduced to have caused the alteration. The first has microthermometric properties (Fig. 3B, field 1) that are very similar to the spilite fluids reviewed above (Fig. 3A, field 1). Quartz within the massive epidosites contains primary and pseudosecondary aqueous LV inclusions with salinities of 3–7 wt.% $NaCl_{eq}$ and T_h(LV→L) between 200 and 410 °C (Richardson et al., 1987; Schiffman and Smith, 1988). Essentially identical inclusions are present in epidote–quartz veins that cross-cut nodular massive epidosites in the Semail SDC (1.6–5.7 wt.% $NaCl_{eq}$; T_h = 258–396 °C; Nehlig and Juteau, 1988) and in a breccia of quartz-cemented epidotized clasts from the Oceanographer Transform fault, Mid-Atlantic Ridge (3.2–8.0 wt.% $NaCl_{eq}$; Vanko et al., 1992). Identical secondary inclusions occur in epidotized plagiogranites in Troodos, but their timing with respect to the epidotization is unclear (Kelley and Robinson, 1990).

The second type of inclusions associated with epidosites are hypersaline (LVH) brines and coexisting, low salinity vapor-dominated LV inclusions. Cowan and Cann (1988) reported such inclusions in quartz and epidote in an epidotized plagiogranite in the Troodos SDC, and interpreted them as the product of liquid–vapor separation of seawater.

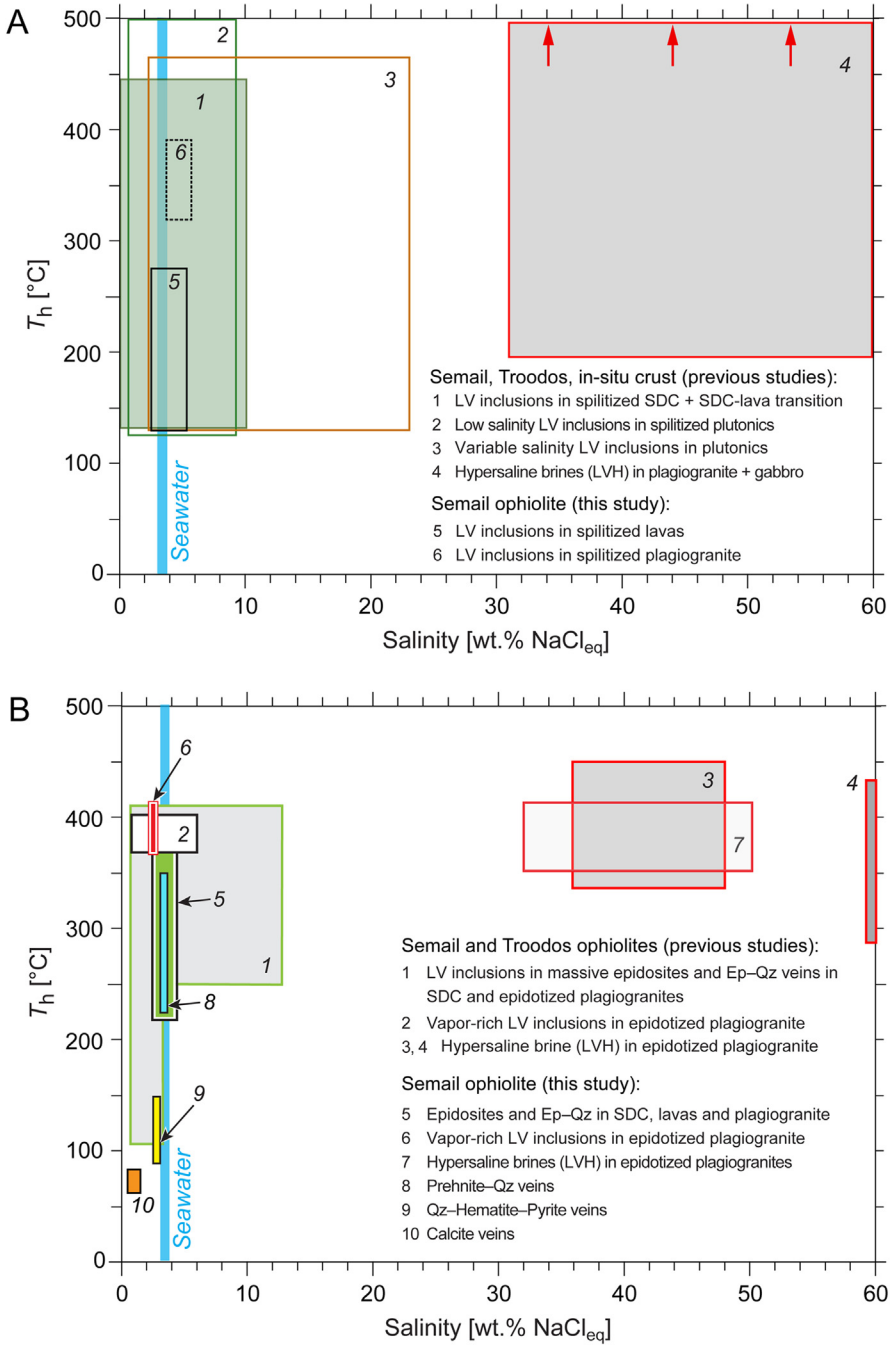

Fig. 3. Fluid inclusion salinities versus homogenization temperatures (T_h) from the literature and this study: (A) Spilite fluids in lavas, sheeted dikes and plutonics: *1*) Gallinatti, 1984; Delaney et al., 1987; Kelley et al., 1992; Saccocia and Gillis, 1995; Gillis, 2002, Heft et al., 2008; Alt et al., 2010; Castelain et al., 2014. *2*) Nehlig, 1989, 1991; Vanko et al., 1988, Vanko et al., 1992; Kelley and Früh-Green, 2001; Alt et al., 2010; Castelain et al., 2014. *3*) Kelley et al., 1992; Vanko et al., 1992; Kelley and Früh-Green, 2001; Castelain et al., 2014. *4*) Hypersaline brines, not necessarily associated with spilite alteration, are shown for reference (Kelley et al., 1992; Vanko et al., 1988, Vanko et al., 1992; Alt et al., 2010; Castelain et al., 2014; Bali et al., 2020). (B) Epidosite fluid and later vein fluids: *1*) Richardson et al., 1987; Schiffman and Smith, 1988; Bettison-Varga et al., 1995; Nehlig et al., 1994; Nehlig and Juteau, 1988. *2*) Kelley et al., 1992; Cowan and Cann, 1988. *3, 4*) Kelley et al., 1992; Cowan and Cann, 1988; Richardson et al., 1987; Juteau et al., 2000. Abbreviations: LV – liquid–vapor; LVH – liquid–vapor–halite; Ep – epidote; Qz – quartz; SDC – sheeted dike complex.

Detailed petrographic descriptions were not provided. Identical fluid inclusions were found by Kelley and Robinson (1990) and Kelley et al. (1992) in small epidosite pods in the Troodos plagiogranites and were contrastingly interpreted to represent magmatic fluids exsolved from the plagiogranite magma. The same high salinity inclusions occur in epidote–quartz veins in epidotized axial plagiogranites in the Semail SDC (Juteau et al., 2000). Juteau et al. (2000) attributed the origin of the hypersaline brines to unmixing of seawater or to magmatic exsolution, and suggested that the fluids fed the Semail VMS deposits during axial spreading. These findings and interpretations are discussed in light of our new evidence in Section 6.4.

4. FLUID INCLUSION METHODOLOGY, SAMPLING AND ANALYTICAL METHODS

Compared to the previous studies reviewed above, the present work employs a modified methodology and additional analytical methods, as follows.

4.1. Fluid inclusion methodology

Our approach to identify inclusions that trapped the spilitizing and epidotizing fluids involves the following four steps. First, we have confined our analyses to groups of fluid inclusions that can be proven to be coeval based on direct petrographic evidence at the thin-section scale. Such demonstrably coeval groups are termed "fluid inclusion assemblages" (Diamond, 1990). Comparing the properties of several inclusions in an individual assemblage provides the basis to recognize and disregard any inclusions modified by post-entrapment processes (e.g., necking down, Roedder, 1981) and to identify the phase state of the fluid during trapping. Thus, assemblages of unmodified inclusions that display uniform phase-volume proportions at laboratory temperature are interpreted to have been trapped from a pore fluid that consisted of a single fluid phase ("homogeneous entrapment"). In contrast, assemblages of inclusions that display variable phase-volume proportions are interpreted to have been trapped from a pore fluid that contained two or more immiscible phases ("heterogeneous entrapment"; see Diamond, 2003 for principles).

Second, we have used the petrographic criteria in Roedder (1984) to established the relative ages of fluid inclusion assemblages with respect to host-mineral growth: primary in crystal growth zones, secondary in post-growth healed fractures, and pseudosecondary in syn-growth healed fractures. As any fracture through a crystal can terminate by chance at an internal growth horizon when viewed in a petrographic section, we have taken care to classify healed fractures as pseudosecondary only when several fractures can be seen terminating at the same growth horizon.

Third, to make mineral growth zonation visible and thereby permit recognition of primary inclusion assemblages, we have applied a variant of SEM-cathodoluminescence (CL) petrography using a secondary electron detector under variable pressure ("VPSE imaging"; Lambrecht and Diamond, 2014). This technique reveals growth zonation in quartz caused by variations in contents of trace elements and other defects that generate luminescence under the electron beam of the SEM (e.g., Götte et al., 2011).

Fourth, we recognize that the studied ophiolites have undergone protracted histories of water–rock interaction and brittle deformation during sub-seafloor hydrothermal alteration and subsequent obduction and exhumation, as evidenced by later generations of hydrothermal veins that cross-cut the spilites and epidosites. To ensure that we can distinguish later fluid inclusions from those that were trapped during the alteration events of interest, we have established in the field the sequence of vein generations in the upper crust of the Semail ophiolite and we have analyzed primary or pseudosecondary fluid inclusions in each vein generation.

4.2. Sampling

Locations of the Semail samples analyzed in this study are shown in Fig. 1. Their volcanostratigraphic and outcrop settings are shown in Figs. 2 and 4, and details are listed in Tables 1 and Supplementary Material 1. To characterize spilite fluids in the Semail ophiolite we sampled quartz ± chlorite-bearing amygdales in spilitized Geotimes lavas, and quartz-bearing miarolitic cavities in spilitized axial and post-axial plagiogranites. For the epidosite fluids we sampled massive epidosite and associated epidote–quartz veins within the SDC (including the localities sampled by Nehlig, 1994, and Nehlig and Juteau, 1988), within the Geotimes pillow lavas (at localities described by Gilgen et al., 2016), and within locally epidotized axial and post-axial plagiogranites (including localities sampled by Juteau et al., 2000). The sampled massive epidosites are of the rarer end-member type, consisting of epidote, quartz, titanite and Fe-oxides, with virtually no relict Mg-bearing minerals inherited from the precursor spilites. Although most of the sampled rocks are of axial magmatic age, it is important to realize that some of the sampled spilite alteration and most of the sampled epidosite alteration occurred during post-axial magmatism.

In addition to the spilites and epidosites, we sampled all the known generations of cross-cutting (post-epidosite) hydrothermal veins: prehnite–quartz veins, quartz–hematite–pyrite (Q') veins, and calcite veins (Table 1; details in Supplementary Material 1).

For comparison with the Troodos ophiolite we visited the sites of earlier studies and obtained epidosites from SDC locality 5 of Richardson et al. (1987; our sample Co51) and from epidotized miarolitic cavities in the altered plagiogranite 0.5–1 km east of Platanistasa sampled by Cowan and Cann (1988) and by Kelley et al. (1992; their locality 9; our sample LR18-Tr06), as detailed in Supplementary Material 1.

4.3. Analytical methods

4.3.1. Optical petrography

Thin sections and doubly-polished thick sections were examined petrographically using an Olympus BX51 polarizing microscope equipped with a range of objective lenses

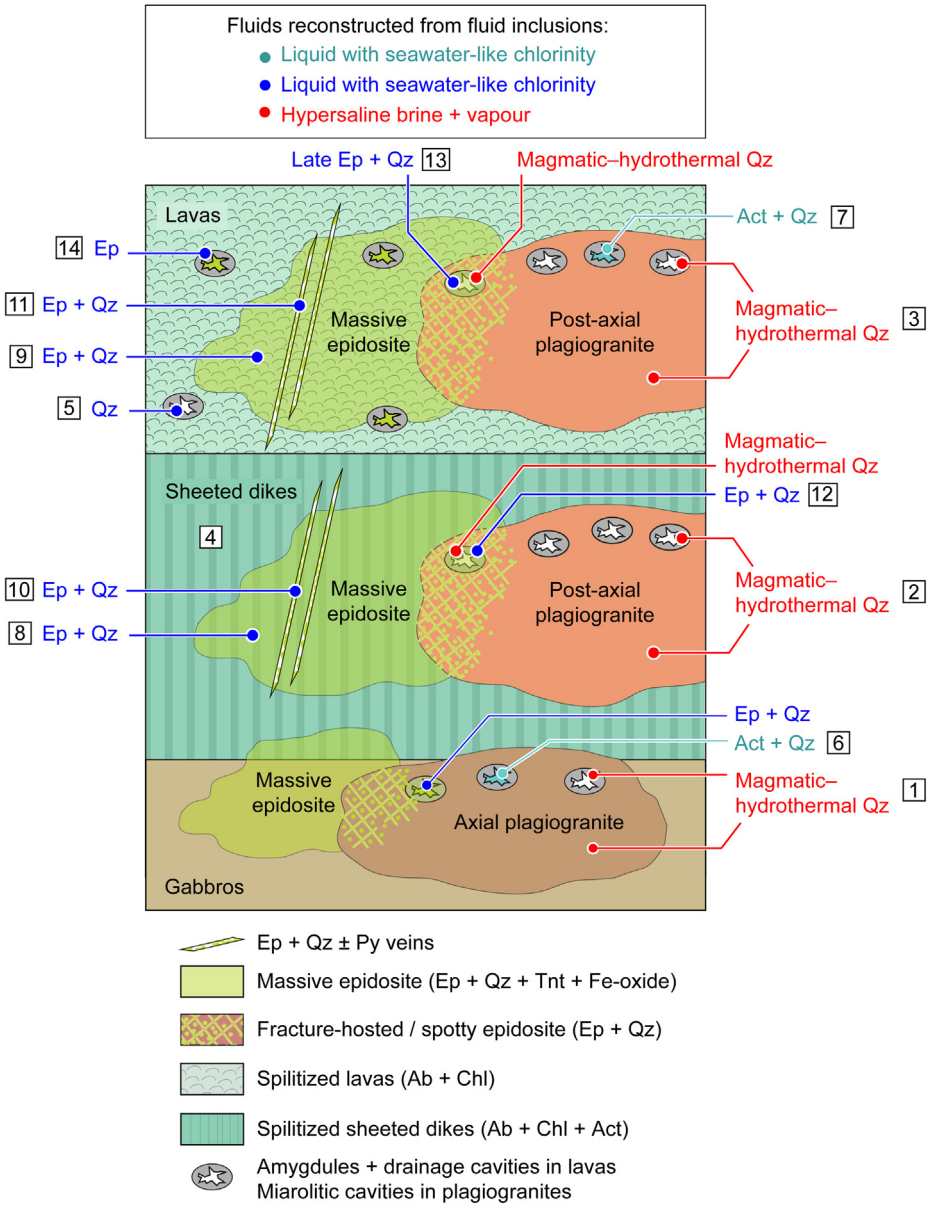

Fig. 4. Schematic vertical stratigraphy in the Semail ophiolite from the lower crustal gabbros up through the sheeted dike complex to the overlying lavas, showing the outcrop settings and types of samples used in this study. Numbers 1 to 14 refer to sample type numbers in Table 1. Abbreviations: Ep – epidote; Qz – quartz; Act – actinolite; Py – pyrite; Tnt – titanite; Hem – hematite; Ab – albite; Chl – chlorite.

up to 100x, and an Olympus UC90 digital camera. In order to interpret the phase state at fluid trapping, the variation in volume fractions of vapor (denoted φ_{vap}) and of captured solids (φ_{solid}) within each assemblage was recorded by estimating the approximate area fraction of the phases. These interpretations were later checked against the spread in homogenization temperatures of each assemblage, which directly and accurately reflects the spread in φ_{vap} values (Bakker and Diamond, 2006; Diamond, 2003).

4.3.2. Cathodoluminescence (SEM-VPSE) imaging

Uncoated, polished thin- and thick sections were used for CL imaging following the SEM-VPSE method of Lambrecht and Diamond (2014). A Zeiss EVO 50 Environmental Scanning Electron Microscope (SEM) was used to acquire grey-scale images of the CL intensity generated by a 14 kV, 2nA electron beam with a spot size of ~500 nm diameter, under 12 Pa air pressure.

4.3.3. Fluid inclusion microthermometry

Microthermometry was performed on doubly polished rock sections of ~80–200 μm thickness using a Linkam THSG 600 heating–freezing stage mounted on an Olympus BX 51 microscope equipped with an Olympus 100x LMPlanFL objective lens of 0.95 NA and a matching substage condenser. The stage was calibrated against phase

Table 1
Name, type and characteristics of samples from the Semail (Oman) and Troodos (Cyprus) ophiolites analyzed in this study.

Sample type	Timing	Fluid generation	Sample/ rock type	Stratigraphic level	Location*	Sample number	Mineral assemblage
1	Pre-epidosite	Magmatic–hydrothermal	Axial plagiogranites	Isotropic gabbro	Wadi Rajmi	LR-WR-T01	Amp+Qz+Pl
			Axial plagiogranite	SDC	Troodos	LR18-Tr06	Amp+Qz+Pl
			Axial plagiogranite	SDC	Troodos	LR18-Tr15	Amp+Qz+Pl
2	Pre-epidosite	Magmatic–hydrothermal	Post-axial plagiogranites	SDC	Wadi Hawqayn	LR18-WH-T02	Amp+Qz+Pl+Ilm
			Post-axial plagiogranites	SDC	Jiltah	LR17-J-T05	Amp+Qz+Pl+Ilm
3	Pre-epidosite	Magmatic–hydrothermal	Post-axial plagiogranites	Lavas	Wadi Bani Umar North	LR17-BUN-Ta	Amp+Qz+Pl+Ilm
			Post-axial plagiogranites	Lavas	Aarja-Bayda	LR17-AB-T07	Amp+Qz+Pl+Ilm
			Post-axial plagiogranites	Lavas	Lasail South	LR-TT-06	Amp+Qz+Pl+Ilm
4	Pre-epidosite	Spilite	Dike	SDC	Wadi Hawqayn	AB17-32c	Act+Chl+Qz
5	Pre-epidosite	Spilite	Amygdale in pillow rim	Lavas	Highway 7, km 15	LR17-BU-Sp02	Qz+Chl+Pmp+Ep in amygdales
			Amygdale in pillow rim	Lavas	near Highway 7, km 15	AB16-4233	Qz+Chl+Pmp+Ep in amygdales
5	Pre-epidosite	Spilite	Lava drainage cavities	Lavas	Rusays	LR17-F-Ep03	Qz
6	Pre-epidosite	Spilite	Axial plagiogranite	Isotropic gabbro	Wadi Rajmi	LR-WR-T01	Qz+Act
7	Pre-epidosite	Spilite	Post-axial plagiogranite	Lavas	Wadi Bani Umar North	LR17-BUN-Ta	Qz+Act+Chl+Ep
8	Syn-epidosite	Epidosite	Massive epidosite	SDC	Wadi Hawqayn	LR17-WH-SD-Ep03	Ep+Act+Qz
			Massive epidosite	SDC	Troodos	Co-51	Ep+Chl+Qz
9	Syn-epidosite	Epidosite	Lava drainage cavity in massive epidosite	Lavas	Ajeeb	LR-A-Ep02	Ep+Qz+Tnt+Hem
			Lava drainage cavity in massive epidosite	Lavas	Ajeeb	LR-A-Ep15	Ep+Qz+Tnt+Hem
			Lava drainage cavity in massive epidosite	Lavas	Ajeeb	SG13-20-2	Ep+Qz+Tnt+Hem
			Lava drainage cavity in massive epidosite	Lavas	Ajeeb	LR17-A-Ep02	Ep+Qz+Tnt+Hem
			Lava drainage cavity in massive epidosite	Lavas	Ajeeb	LR17-A-Ep03	Ep+Qz+Tnt+Hem
			Lava drainage cavity in massive epidosite	Lavas	Rusays	LR17-F-Ep03	Ep+Qz+Tnt+Hem
10	Syn-epidosite	Epidosite	Ep–Qz vein	SDC	Wadi Hawqayn	LR17-WH-SD-Ep03	Ep+Qz+Hem
11	Syn-epidosite	Epidosite	Ep–Qz vein	Lavas	Ajeeb	SG13-41	Ep+Qz+Tnt+Hem
12	Syn-epidosite	Epidosite	Miarolitic cavities in post-axial plagiogranite	SDC	Wadi Hawqayn	LR18-WH-T02	Ep+Qz+Hem
			Massive epidosite	SDC	Troodos	LD-CY-8	Ep+Chl+Qz
			Miarolitic cavities in post-axial plagiogranite	SDC	Troodos	LR18-Tr06	Ep+Qz

13	Syn-epidosite	Epidosite	Miarolitic cavities in post-axial plagiogranite	Lavas	Wadi Bani Umar North	LR17-BUN-Ta	Ep+Qz	
14	Syn-epidosite	Distal epidosite	Lava drainage cavity	Lavas	Al Malah	LR-AM-Ep06	Ep	
15	Post-epidosite	Prehnite–quartz	Vein	Lavas	Al Malah	LR-AH-03	Prh+Qz	
			Vein	Axial gabbros and SDC	Wadi Haymiliyah	LR18-WHim-G	Prh	
			Lava drainage cavity	Lavas	Ajeeb (Hatta Extended)	LR18-HE-Ep01	Prh+Qz	
			Vein	Lavas	Ajeeb	220122-7	Prh+Qz	
			Vein	Lavas	Yanqul	SWOM-17-29	Prh+Qz	
16	Post-epidosite	Hematite–quartz ± pyrite	Vein	SDC	Wadi Haymiliyah	LR18-WH-SD-Ep02	Hem+Qz+Chl+Py+Cpy	
			Vein	Lavas	Haduf	260112-11A	Hem+Qz+Chl	
			Vein	Lavas	Ajeeb	LR17-A-Qz01a	Hem+Qz+Chl	
17	Post-epidosite	Calcite–quartz	Vein	SDC	Wadi Hawqayn	LR17-WH-SD-Ep03	Cal+Qz+Hem	
			Vein	Lavas	Ajeeb	LR17-A-Cal02a	Cal+Qz+Hem	

* see Supplementary Material 1 for GPS coordinates; Mineral abbreviations: Act – actinolite; Amp – amphibole; Cal – calcite; Chl – chlorite; Cpy – chalcopyrite; Ep – epidote; Hem – hematite; Ilm – ilmenite; Pl – plagioclase; Prh – prehnite; Pmp – pumpellyite; Py – pyrite; Qz – quartz; Tnt – titanite.

transitions in synthetic, quartz-hosted H_2O and CO_2–H_2O inclusions of known composition and density (melting of solid CO_2 at -56.6 °C, melting of H_2O-ice at 0.0 °C and critical homogenization of H_2O at 374.1 °C). Measurements below room temperature are thus accurate to ±0.1 °C and those above room temperature are accurate to ±1.5 °C.

All the analyzed inclusions contain aqueous liquid (L) and aqueous vapor (V) phases at laboratory temperature (T_{lab}), and some contain solids (e.g., halite, H). Halite was identified by its reaction with H_2O to form hydrohalite at low temperature, by the absence of a meniscus where it touches the ordinary optical axis of quartz, and by its absence of a Raman spectrum. After first cooling the inclusions to -190 °C, two equilibrium phase transitions were measured upon gradual heating at 0.5 °C/min: (1) the temperature at which the last crystal of ice melts in the presence of liquid and vapor, denoted T_m(Ice); (2) the temperature at which the inclusion phases homogenize. In LV inclusions dominated by liquid at T_{lab} this corresponds to a bubble-point transition via shrinkage and disappearance of the vapor bubble, denoted T_h(LV→L). In LV inclusions dominated by vapor at T_{lab}, homogenization occurs via expansion of the vapor bubble in a dew-point transition, denoted T_h(LV→V). Usually only a minimum constraint can be placed on the dew-point temperature, owing to disappearance of the L–V meniscus into the dark inclusion walls as the true homogenization temperature is approached. All inclusions were checked for the presence of gas-clathrates at temperatures above T_m(Ice).

The salinity of the inclusions based on microthermometry alone is expressed in NaCl equivalent concentration (wt. % $NaCl_{eq}$) regardless of the true solute compositions. The salinity of LV inclusions was calculated from T_m(Ice) and the salinity of LVH inclusions was calculated from T_m(H), both using the AqSo_NaCl P–T–V_m–x correlation for the binary H_2O–NaCl system in Bakker (2018; based on Driesner and Heinrich, 2007; Driesner, 2007).

4.3.4. Laser Raman analyses of fluid inclusions

Laser Raman analyses were conducted on a confocal Jobin Yvon Horiba microprobe (LABRAM HR-800) equipped with an Olympus BX41 microscope. A 532.12 nm laser was focused through an Olympus 100x UMPlan FL objective to obtain a beam spot on the sample of ~20 mW power and ~1 μm diameter.

Vapor bubbles in fluid inclusions were scanned for gas species, including H_2O, CH_4, CO_2, H_2 and H_2S, at a spectral resolution of 2 cm^{-1} with ≥20 s acquisition time. The identity of the final solid phase to melt upon warming the inclusions from sub-zero temperatures was determined by mounting the heating-freezing stage on the Raman microprobe and scanning for the characteristic spectra of ice, hydrohalite ($NaCl{\cdot}2H_2O$) and solid hydrates of $CaCl_2$. Other accidentally trapped solids in the inclusions were identified from their characteristic spectra at room temperature.

4.3.5. Laser-ablation ICP-MS analyses of fluid inclusions

Mass ratios of elements in individual fluid inclusions in quartz were determined by laser-ablation inductively-

Table 2
Mineral–fluid parageneses in seven fluid generations associated with miarolites in axial and post-axial plagiogranites, with spilite and epidosite alteration and with hydrothermal veining in the Semail ophiolite.

	– *Time*→ Fluid generation								
Mineral	Plagiogranite melt	Magmatic–hydrothermal	Spilite	Epidosite	Prh–Qz veins†	Qz–Hem ± Py veins†	Cal–Qz veins†	Salinity [wt.% $NaCl_{eq}$]	T_h [°C]
Plagioclase	——								
Albite		——	——						
K-feldspar	– Rare –								
Amphibole	– Melt incl. –								
Ilmenite	——								
Apatite	——	——	——						
White Qz*	– Melt incl. –								
Med.-grey Qz*		– Brine ± vapor FI –						Brine: ≥ 30	380–410
Dark Qz*			– LV FI –					2.4–4.0	128–390
Dark Qz*				– LV FI –				2.6–3.9	225–370
Twinned Qz*					– LV FI –			3.4–3.7	(220)
Dark Qz*						– LV FI –		2.6–2.9	100–145
Dark Qz*							– LV FI –	0.5–1.9	62–81
Epidote			——	– LV FI –					
Titanite			– LV FI –	——					
Rutile			——						
Magnetite	——		——						
Hematite			——	——		——	——		
Actinolite			– LV FI –						
Chlorite						——			
Prehnite					——				
Calcite									
Pyrite						——			
Seawater								3.1–3.9	

* Degree of brightness in greyscale CL image; Abbreviations: Qz – quartz; Rt – rutile; Hem – hematite; Prh – prehnite; LV – liquid-vapor; FI – fluid inclusions; † for details see Supplementary Material 1.

Table 3
Mineral–fluid parageneses in four fluid generations associated with plagiogranite miarolites and with spilite and epidosite alteration in the Troodos ophiolite.

	– *Time* →					
	Fluid generation					
Mineral	Plagiogranite melt	Magmatic–hydrothermal	Spilite	Epidosite	Fluid salinity [wt.% $NaCl_{eq}$]	T_h [°C]
Plagioclase	——					
Albite			——			
K-feldspar	– Rare –					
Amphibole	——					
Ilmenite	——					
Apatite	——	——	——			
White Qz*	– Melt incl. –					
Med. grey Qz*		– Brine+vapor FI –			Brine: >30	340–356
Dark Qz*			– LV FI –		5.7	318–323
Dark Qz*				– LV FI –	3.2	272–283
Epidote				– LV FI –	3.1–3.2	275–280
Titanite						
Magnetite						
Hematite			——	——		
Actinolite			——			
Chlorite			——			
Seawater					3.1–3.9	

* Degree of brightness in greyscale Cl image; Abbreviations: Qz – quartz; LV – liquid-vapor; FI – fluid inclusions.

coupled-plasma mass-spectrometry (LA-ICP-MS). Fluid inclusions in epidote were not analyzed owing to the high background of Ca in the host. A Lambda Physik GeoLas-Pro 193 nm ArF excimer laser system was used in combination with a Perkin Elmer ELAN DRC-e or an Agilent 7900 quadrupole mass spectrometer following the procedure in Pettke et al. (2012). Analyses were made for ^{7}Li, ^{11}B, ^{23}Na, ^{25}Mg, ^{29}Si, ^{35}Cl, ^{39}K, ^{43}Ca, ^{57}Fe, ^{79}Br, ^{85}Rb, ^{88}Sr and ^{137}Ba, as calibrated against the standards GSD-1G (Jochum et al., 2011) and Sca-17 (Seo et al., 2011; Fusswinkel et al., 2018).

Ablation profiles were processed using the SILLS software (Guillong et al., 2008; Figs. S10, S11), yielding mass ratios or limits of detection (LOD) where signals are not significant. The LOD values pertain to individual fluid inclusions depending on inclusion size, depth, ablation behaviour, etc. in addition to instrumental settings. For a given element, the lowest LOD among the inclusions analyzed in an assemblage is accordingly the most relevant. Nevertheless, if the inclusion with the lowest LOD has unfavorable fluid inclusion properties, its calculated LOD may exceed the element concentration derived from other inclusions with statistically significant element signals. Occasional outliers were filtered from the final data set by applying the conventional Extreme Studentized Deviation test, which assumes Gaussian distribution. To avoid skewing, median values are used where eight or less inclusions were accepted per fluid inclusion assemblage. Since Na is the dominant cation in all the analyzed inclusions, and since the element concentrations in the inclusions can be later calculated using the known $NaCl_{eq}$ salinity determined by microthermometry, the relative concentrations of the analytes are expressed as mass ratios with respect to Na.

4.3.6. Calculation of bulk fluid inclusion compositions

For the samples that yielded useful element ratios by LA-ICP-MS, bulk fluid compositions were calculated as follows. Since Cl, Na and Ca dominate all inclusions with salinities $\leq$5.3 wt.% $NaCl_{eq}$ (Section 5.3), and since the precision of the Cl analyses is too limited to constrain charge-balance, the analyzed cations were artificially balanced with chloride and then grouped into 1:1 versus 1:2 chloride salts. Owing to the low salinities of these inclusions and to the dominance of Na and Ca, it can be assumed that the 1:1 salts have the same colligative properties as NaCl and that the 1:2 salts have the same properties as $CaCl_2$ (Figs. S12 and S13). The concentrations of the solutes were then calculated from the ratio of salt types plotted on the relevant T_m(Ice) isotherm in the H_2O–NaCl–$CaCl_2$ model system, using the liquidus diagram of Steele-MacInnis et al. (2011). This calculation also permitted conversion of $NaCl_{eq}$ into salinity in terms of total dissolved solids (TDS).

In the hypersaline (LVH) inclusions the cations were similarly balanced with Cl and grouped into 1:1 and 1:2 salts. The dominant solutes are Cl, Na and K but there is also significant Fe. To account for the colligative effects of Fe on the 1:2 group, the mass ratio of salt groups was plotted on the relevant T_m(H) isotherm of the H_2O–NaCl–$FeCl_2$ model halite liquidus (Lecumberri-Sanchez et al., 2015), thereby permitting calculation of bulk solute concentrations (Fig. S14).

5. RESULTS

5.1. Petrography of altered upper crustal rocks

The following petrographic descriptions provide the mineralogical and temporal context for the fluid inclusion

analyses presented in Section 5.2. Emphasis is placed on identifying the temporal sequence of hydrothermal mineral assemblages in each of the sampled rock units. Tables 2 and 3 summarize the paragenetic sequences comprising the alteration types observed in the Semail and Troodos ophiolites, revealing the mineral assemblages coeval with the analyzed fluid inclusions.

5.1.1. Sheeted Dike Complex (SDC)

Most dikes in the SDC are spilitized diabases (Nehlig et al., 1994; Miyashita et al., 2003) displaying alteration assemblages involving albite + chlorite with varying amounts of hydrothermal actinolite and minor quartz, epidote, titanite and magnetite. Relict igneous augite and titanomagnetite are often preserved. This assemblage is locally completely replaced by massive, granoblastic epidosites (Fig. 5A) comprising intergrowths of euhedral epidote and quartz with accessory titanite and hematite or occasionally magnetite, often containing relicts of spilitic actinolite (Nehlig, 1989; Gilgen et al., 2016). Associated epidote–quartz veins up to 2 cm wide cross-cut the massive epidosite bodies and the adjacent spilites (Fig. 5B). The veins are mostly compact but locally vuggy, consisting of coevally grown euhedral epidote and quartz. These minerals are often partially overgrown by later, genetically unrelated calcite and quartz. This late quartz is readily distinguished from the epidote-generation quartz by petrographic criteria.

5.1.2. Lavas

Spilitized Geotimes pillow lavas consist of hydrothermal chlorite + albite + titanite + hematite ± quartz ± epidote ±

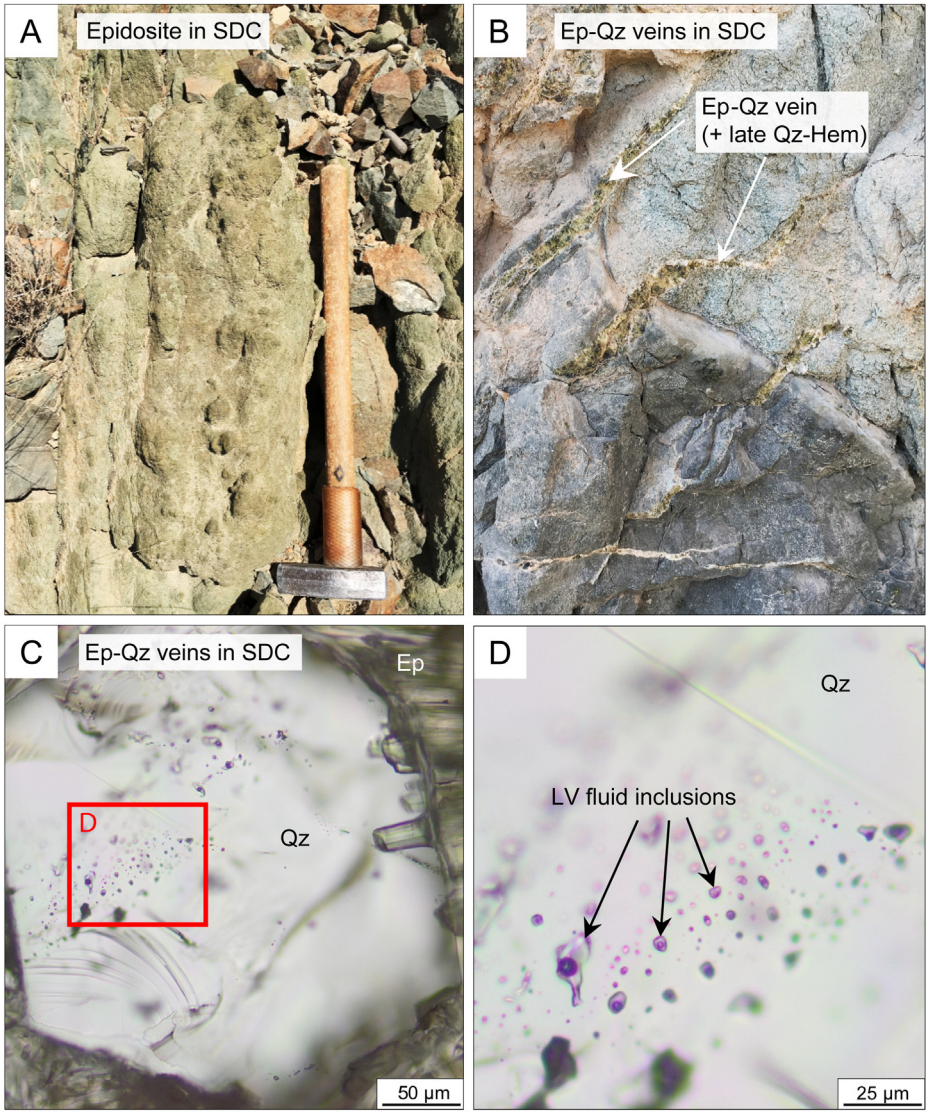

Fig. 5. Field and microphotographs of massive epidosites in dikes of the SDC and associated cross-cutting Ep–Qz veins (Sample: LR17-WH-SD-Ep03) from the Semail ophiolite. (A) Completely epidotized dike core. (B) Epidotized dikes hosting Ep–Qz veins cross-cut by later Qz-Hem and calcite veins. (C) Close-up of an Ep–Qz vein with euhedral Ep + Qz. (D) Close-up of (C): Secondary, homogeneously trapped LV fluid inclusions in quartz. Abbreviations: Ep – epidote; Qz – quartz; Hem – hematite; SDC – sheeted dike complex.

submicroscopic needles of actinolite. Relict igneous augite and titanomagnetite are common but relict plagioclase is only occasionally preserved (Alabaster and Pearce, 1985; Gilgen et al., 2016). Vesicles (mm–cm diameter) are often empty but in certain areas vesicles and lava drainage cavities in the pillows are lined by mm-size euhedral quartz crystals intergrown with chlorite, indicating that they belong to the spilite assemblage (Fig. 6A, B). In spilitized lavas overprinted by weak or intense epidosite, the precursor cavity quartz is often overgrown by euhedral epidote and a second generation of quartz belonging to the epidosite assemblage (Fig. 7A). Where the two generations are present in the same thin section they can be distinguished systematically not only by their mineral intergrowths but also by the slightly brighter CL intensity of the precursor spilite-generation quartz (Fig. 7E). The CL images show that crystal faces of the spilite-generation quartz occasionally underwent partial dissolution prior to being overgrown by epidosite-generation quartz.

Sparse epidote–quartz veins up to 2 cm wide, with the same features as those in the sheeted dikes, cross-cut the epidotized pillows and often reach out into the surrounding spilitized lavas. Post-epidosite fillings of vesicles and drainage cavities include pumpellyite, prehnite and zeolite.

5.1.3. Plagiogranites

The paragenetic sequence of igneous and hydrothermal minerals observed in the Semail plagiogranites is shown in the first two columns of Table 2 (based on petrographic relationships in Figs. S1–S4). The igneous mineral assemblages of the axial and post-axial plagiogranites are very similar. Both consist of plagioclase, edenitic amphibole and minor quartz with rare K-feldspar and clinopyroxene plus accessory ilmenite and apatite. Some post-axial plagiogranites also contain magnetite. The interstitial matrix quartz in both generations exhibits bright CL (light-grey to white) typical of igneous quartz in granitoids worldwide (e.g., Landtwing and Pettke, 2005). The quartz is also often intergrown granophyrically with plagioclase. Both quartz and amphibole contain former melt inclusions (now crystallized), as described in Section 5.2.1.

Huge numbers of regularly spaced miarolitic cavities are present in some areas of the plagiogranite stocks. The cavities have equant to lensoid shapes and are up to several cm in diameter. Some elongate cavities are linked to adjacent cavities, but the three-dimensional outcrop conditions are clear enough to conclude that the majority of cavities are unconnected. The cavities are bordered by pegmatitic intergrowths of coarse igneous plagioclase and quartz, containing almost none of the edenitic amphibole that otherwise makes up about 20 vol.% of the plagiogranite matrix. The cavities are partly filled by freely grown hydrothermal actinolite and euhedral quartz. The cores of the quartz crystals contain apatite and melt inclusions and exhibit intense CL, as does igneous quartz in the rock matrix.

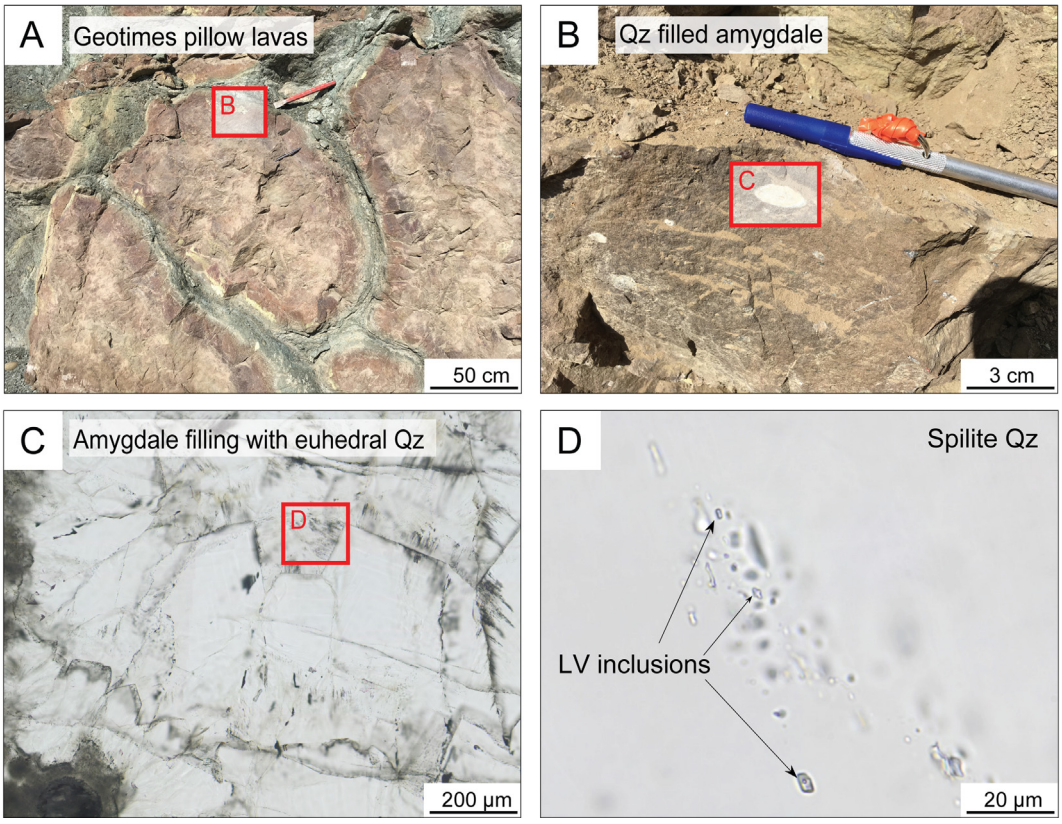

Fig. 6. (A, B) Field photographs of spilite-generation quartz in amygdales in Geotimes lavas. (C) Close-up of B: Microphotograph of amygdale quartz with growth zonation. (D) Primary LV fluid inclusions along quartz growth zone. Abbreviations: Qz – quartz; LV – liquid-vapor.

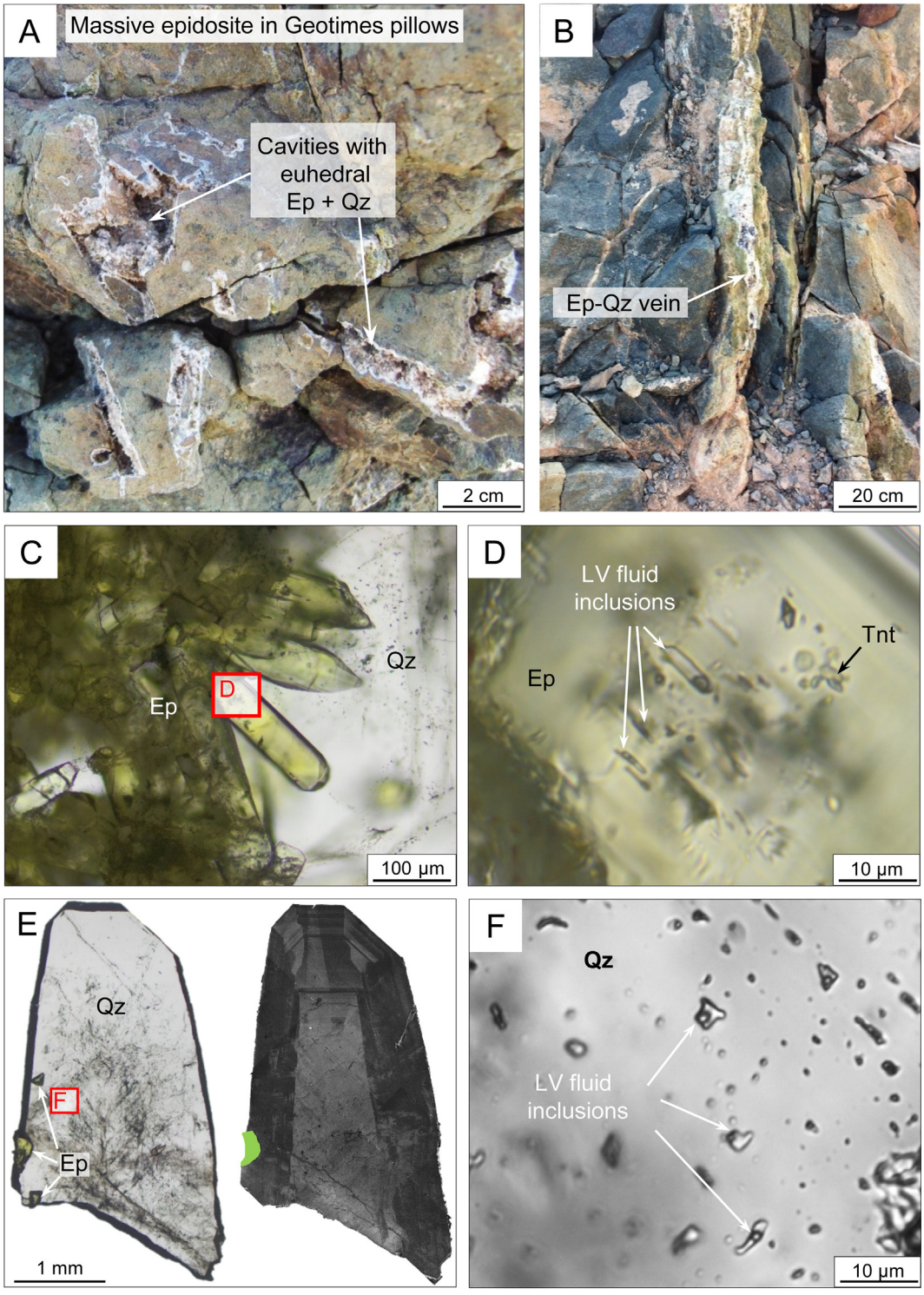

Fig. 7. Field and microphotographs of massive epidosites in axial Geotimes lavas and associated Ep–Qz veins in the Semail ophiolite: (A) Lava drainage cavities filled with euhedral Ep + Qz (Sample: LR17-A-Ep03). (B) Ep–Qz vein in massive epidosite overprinted by a later Hem–Qz vein assemblage (Sample: SG13-41). (C) Euhedral Ep crystals in Ep–Qz veins containing (D) primary LV fluid inclusions. (E) Transmitted light and SEM-VPSE image of euhedral Qz + Ep and (F) pseudosecondary LV inclusions with uniform vapor fractions. Abbreviations as in Figs. 5 and 6.

Both the igneous quartz crystals in the matrix and in the miarolitic cavities are epitaxially overgrown by quartz with medium-grey CL that we refer to as "magmatic–hydrothermal". The igneous quartz shows CL evidence for partial dissolution prior to being overgrown by the magmatic–hydrothermal quartz. Elongate apatite is the

only other mineral we have found coeval with the magmatic–hydrothermal quartz.

All the plagiogranites are to some degree pervasively spilitized, as manifested by alteration of plagioclase to albite, of clinopyroxene and igneous amphibole to hydrothermal actinolite and chlorite, and of magnetite and ilmenite to titanite, hematite and rarely rutile. Hydrothermal quartz is also part of the spilite assemblage, most notably overgrowing magmatic–hydrothermal quartz epitaxially in the miarolitic cavities. This spilite-generation quartz is dark in CL images, allowing the three generations of quartz to be distinguished. The CL of the spilite-generation quartz reveals that it also occurs pervasively in the rock matrix as coatings or fillings of microfractures within the earlier quartz generations. Magmatic–hydrothermal quartz shows no signs in CL of dissolution prior to being overgrown by spilite-generation quartz. In contrast, discordant embayments in the subtle growth zoning in the spilite quartz shows that it was partly dissolved prior to being overgrown by epidosite-generation quartz (as observed in the lava-hosted epidosites, Section 5.1.2).

Epidosite alteration consisting of epidote + quartz + titanite ± hematite ± rutile locally overprints spilite alteration in the plagiogranites (Fig. S2). The epidosite minerals are most obvious as fillings in the miarolitic cavities (Fig. 8), overgrowing the spilite minerals where present. Patchy epidosite alteration throughout the plagiogranite matrix is common and is often accompanied by rectilinear networks of cooling joints filled by epidote + quartz.

The paragenetic sequence of igneous and hydrothermal minerals in our samples of the axial plagiogranite at Platanistasa, Troodos (Table 3), is essentially identical to that of the Semail plagiogranites. Igneous quartz in the rock matrix is graphically intergrown with plagioclase (albitized by spilite alteration) and hosts isolated melt inclusions. Precisely as observed in the Semail samples, the quartz lining the miarolitic cavities exhibits four stages of quartz overgrowths with characteristic textures and CL intensities defining igneous, magmatic–hydrothermal, spilite and epidosite generations, with slight dissolution of quartz prior to precipitation of the epidosite generation (Fig. S6).

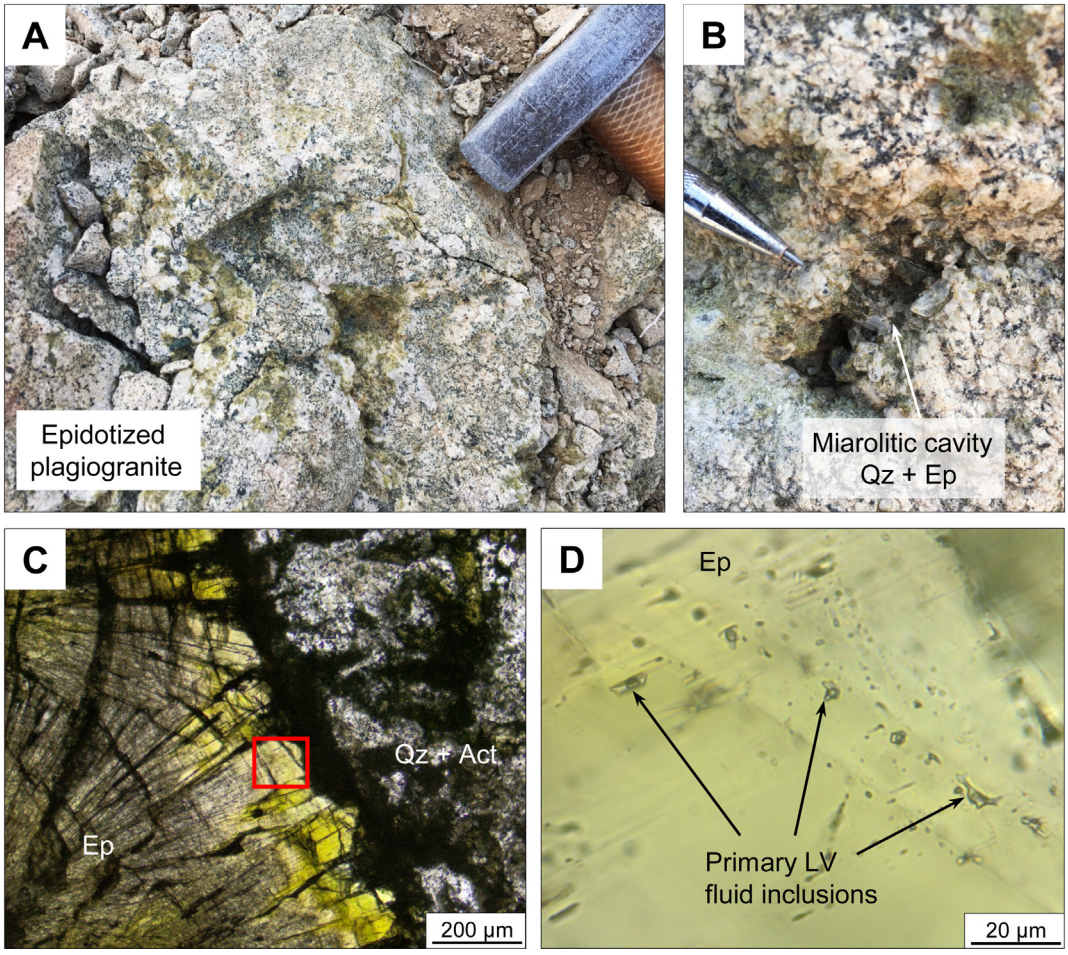

Fig. 8. Field- and micro-photographs of epidotized post-axial plagiogranite at Bani Umar North, Semail ophiolite (Sample: LR17-BUN-Ta): (A, B) Local patchy matrix epidotization and miarolitic cavities filled with Qz+Ep. (C) Euhedral Ep in miarolitic cavity with (D) primary LV fluid inclusions along crystal growth zones. Abbreviations as in Figs. 5 and 6.

5.2. Characterization of fluid generations by fluid inclusion petrography and microthermometry

A total of 77 thin- and thick-sections from 11 locations in the Semail ophiolite and 10 sections from five locations in the Troodos ophiolite were examined petrographically for their fluid inclusions. Tables 2 and 3 show the types of primary fluid inclusions found within their cogenetic host minerals. The salinities and homogenization temperatures are summarized in Tables 2 and 3, and detailed compositional results are given in Table 4. The complete microthermometric data can be found in the Research Data.

In general, primary or pseudosecondary fluid inclusions with tractable sizes are quite rare in the Semail spilites and epidosites and only few of the many samples we collected contain unequivocal petrographic relations that prove the relative timing of inclusion trapping. Hydrothermal minerals that formed at higher temperatures, e.g., in cooling plagiogranites, tend to have the most abundant primary inclusions. The fluid inclusion petrographic and microthermometric results pertaining to each generation are presented below in the order of their relative age with respect to the local (outcrop-scale) timing of massive epidosites, i.e., pre-, syn-, and post-epidosite.

5.2.1. Pre-epidosite melt inclusions in plagiogranites

In miarolitic cavities in the post-axial Semail plagiogranites (e.g., Bani Umar North and Wadi Hawqayn), igneous quartz hosts assemblages of primary inclusions consisting of numerous birefringent crystallites with only minor aqueous vapor ($\varphi_{vap} \sim 0.25$) and aqueous liquid ($\varphi_{liq} \sim 0.05$) (Fig. 9D1, D2). Based on Raman analysis, many of the crystallites are silicates, including amphibole. The volumetric proportions of the phases in the inclusions are uniform within individual assemblages, indicating homogeneous entrapment and implying that the solids are daughter minerals. The homogeneous entrapment and dominance of silicate daughters indicate that the inclusions were initially droplets of silicate melt. Following their entrapment in quartz they exsolved a little aqueous liquid and vapor and the remainder of the melt crystallized into the various daughter minerals. These inclusions are labelled "melt inclusions" in Table 2. The Platanistasa axial plagiogranite in Troodos (e.g., sample LR18-Tr06) contains the same kind of melt inclusions (Table 3).

5.2.2. Pre-epidosite, magmatic–hydrothermal fluid in plagiogranites

In the Semail axial plagiogranite at Wadi Rajmi, locally epidote-free miarolitic cavities contain magmatic–hydrothermal quartz that fills fractures in the earlier precipitated igneous quartz. These healed fractures contain pseudosecondary assemblages of very small (≤5 μm diameter) aqueous LVH inclusions, which represent the fluid that precipitated the magmatic–hydrothermal quartz. Halite dominates the inclusions ($\varphi_{hal} \sim 0.4$) with subordinate vapor ($\varphi_{vap} \sim 0.2$), aqueous liquid ($\varphi_{liq} \sim 0.3$) and minor amounts of hematite (presumably former magnetite transformed by leakage of H_2) and other unidentified solids. The uniform phase proportions indicate homogeneous entrapment of a dense hypersaline liquid. The inclusions (Fig. S1F) tend to leak and decrepitate upon heating above 400 °C. No reliable data could be obtained by microthermometry.

In the post-axial Semail plagiogranites (e.g., Lasail South, Bani Umar North, Wadi Hawqayn), magmatic–hydrothermal quartz in the miarolitic cavities contains some primary but mostly pseudosecondary assemblages of heterogeneously trapped inclusions, varying from a hypersaline LVH endmember to a vapor-rich LV endmember (Fig. 9E1, E2). The hypersaline brines ($\varphi_{vap} \sim 0.3$; $\varphi_{hal} \sim 0.3$) show different sequences of phase transitions upon heating. Some assemblages undergo halite melting via LVH→LV at 210–365 °C prior to homogenization via LV→L at 380–453 °C (e.g., in the Wadi Hawqayn and Lasail South plagiogranites). Other assemblages show the reverse order: LVH→LH at 231–270 °C and LH→L at 355–420 °C. All these inclusions contain over 30 wt.% $NaCl_{eq}$, whereas the coexisting vapor-rich inclusions (Fig. 9E2) contain 2.4–4.2 wt.% $NaCl_{eq}$. Upon heating, the vapor-rich inclusions show expansion of their bubbles as they approach a dew-point transition (LV→V), but precise transition temperatures could not be measured owing to migration of the L–V meniscus into the dark rims of the inclusions.

In miarolitic cavities in the Platanistasa axial plagiogranite, Troodos (e.g., sample LR18-Tr06), magmatic–hydrothermal quartz contains assemblages of primary, LVH inclusions and coexisting LV inclusions with variable vapor fractions distributed in 3D clusters (Fig. S6B–D). Similar assemblages are present along healed fractures. No clear endmember vapor-rich inclusions were found. Microthermometry of LVH inclusions in two fluid inclusion assemblages reveal T_m(LVH→LV) of 290–330 °C (implying ~40 wt.% $NaCl_{eq}$) and T_h(LV→L) of 340–375 °C. The Troodos inclusions are thus very similar to the Semail inclusions.

5.2.3. Pre-epidosite spilite fluid in axial lavas and in plagiogranites

Euhedral quartz in lava drainage cavities (e.g., in Geotimes lavas at Rusays), which was locally overgrown by epidote and quartz during later pervasive epidosite alteration, hosts primary, homogeneously trapped assemblages of aqueous fluid inclusions with $\varphi_{vap} \sim 0.06$. These inclusions contain 2.4–2.6 wt.% $NaCl_{eq}$ and T_h(LV→L) values are 128–140 °C. Presumably this pre-epidosite quartz belongs to the spilite alteration assemblage.

In spilitized Geotimes lavas distant from any epidosite or post-epidosite veins, the only amygdale quartz that we found with tractable primary fluid inclusions occurs alone without other coeval minerals, although it sits on earlier chlorite. Whether the quartz belongs to the main albite + chlorite + quartz spilite alteration or to the later prehnite + quartz generation (see Supplementary Material 1) is therefore unclear solely from petrographic relations. The euhedral quartz crystals in the amygdales host primary, aqueous LV inclusions in homogeneously trapped assemblages (φ_{vap} is uniform within each assemblage, with values for different samples and assemblages varying between 0.1

Table 4
Summary of microthermometric analyses of fluid inclusions in this study.

Fluid generation	Sample type	Sample number	Host mineral	Fluid inclusion origin	Trapping state	Phases at T_{lab}	φ_{Vap}	T_m(Ice) or T_m(Halite)[1] [°C]	Salinity [wt.% $NaCl_{eq}$]	T_h(LV→L) or T_h(LVH→LH)[2] [°C]
Pre-epidosite fluid generations										
Magmatic–Hydrothermal	Plagiogranite and miarolitic cavities	LR17-BUN-Ta	Qz	P	Hom	LV+ solids	0.4	-	-	-
			Qz	PS	Het	LVH	0.3	355–373[1]	48–50	263–273[2]
						LV	0.9	-1.6 to -1.4	2.6–2.9	-
	Miarolitic cavities in plagiogranite	LR18-WH-T02	Qz	P	Het	LVH	0.3	210–223[1]	32–33	380–410
		LR18-Tr06*	Qz	PS	Het	LVH	0.3	290–330	39	340–375
						LV	0.9	n.d.	-	n.d.
		LR-TT06	Qz	P	Het	LVH	0.3	340–365	43	422–453
						LV	0.9	-2.5 to -2.2	4.0	n.d.
Spilite	Miarolitic cavities in plagiogranite	LR17-BUN-Ta	Qz	P	Hom	LV	0.6	-2.4 to -2.2	3.8–4.0	380–390
		LR18-Tr06b*	Qz	P	Hom	LV	0.2	-3.5 to -2.9	4.8–5.7	318–323
	Amygdales in lavas	LR17-BU-Sp02	Qz	P	Hom	LV	0.1	-1.9 to -1.8	3.1–3.2	160–180
		AB16-4233	Qz	P	Hom	LV	0.2	-2.0 to -1.8	3.2–3.4	265–275
	Cavity in lavas	LR17-F-Ep03b	Qz	P	Hom	LV	0.06	-1.5 to -1.4	2.4–2.6	130–140
Syn-epidosite fluid inclusion generation										
Epidosite	Massive epidosite in SD	LR17-WH-SD-Ep03	Qz	?	PEM/Het?	LV	0.15	-3.1 to -2.8	4.7–5.1	200
						V	0.8	-0.9	1.6	-
			Qz	S	Hom	LV	0.2	-1.8	3.1	250–260
		Co-51*	Qz	P	Hom	LV	0.3	-1.9	3.2	277
	Drainage cavities in massive epidosite in lavas	LR-A-Ep15-Qz2	Qz	PS	Hom	LV	0.25	-1.7 to -1.5	2.6–2.9	280–295
		LR-A-Ep15-Qz7	Qz	PS	Hom	LV	0.25	-1.8	3.1	275–285
		LR-A-Ep02a	Qz	PS	Hom	LV	0.25	-1.9 to -1.8	3.1–3.2	275–280
		SG13-20-2-Qz2	Qz	PS	Hom	LV	0.25	-1.5	2.6	280–290
		SG13-20-2-Qz3	Qz	PS	Hom	LV	0.3	-1.7 to -1.5	2.6–2.9	295–305
		LR17-F-Ep03b Qz3	Qz	PS	Hom	LV	0.25	-2.2 to -2.0	3.4–3.7	270–295
		LR17-F-Ep03b Qz4	Qz	P	Hom	LV	0.15	-2.3 to -2.0	3.4–3.9	220–240
		LR18-Tr06*	Qz	P	Hom	LV	0.3	-3.1 to -3.0	5.0–5.1	380–390
	Epidote–quartz veins	LR17-WH-SD-Ep03	Ep	P	Hom	LV	0.2	-1.9 to -1.7	2.9–3.2	250–260
		SG13-41	Ep	P	Hom	LV	0.3	-2.3 to -2.1	3.6–3.9	300–315
	Epidotized miarolitic cavities in plagiogranite	LR17-AB-T07b	Ep	P	Hom	LV	0.25	-2.4 to -2.3	3.9–4.0	365–370
		LR18-Tr15*	Ep	P	Hom	LV	0.2	-2.3 to -2.2	3.6–3.9	358–369
		LR18-Tr-T06*	Ep	P	Hom	LV	0.2	-3.1 to -3.0	5.0–5.1	275–280
		LR17-BUN-Ta	Qz	P	Hom	LV	0.2	-1.9 to -1.8	3.1–3.2	252–256
	Lava drainage cavity	LR-AM-Ep06	Ep	P	Hom	LV	0.25	-1.9 to -1.8	3.1–3.2	275–280

Post-epidosite fluid generations †										
Quartz–hematite–pyrite	Vein	260112-11A	Qz	P	Hom	LV	0.1	-1.6 to -1.5	2.4–2.7	144–145
		LR-A-Ep17	Cal	P	Hom	LV	0.05	-1.1 to -1	1.7–1.9	75–81
Prehnite–quartz	Vein	LR17-AH-03	Qz	P? (Isolated)	?	LV	??	-2.2 to -2.0	3.4–3.7	220
Calcite	Vein	LR17-A-Cal02	Cal	S	Hom	LV (or mono-phase L)	0.05	-0.3 (mostly metastable)	0.21	62–78
		LR17-WH-SD-Ep03	Qz	P	Hom	LV	0.07	-0.4 to -0.2	0.4–0.7	56–72

Abbreviations: Cal – calcite; Ep – epidote; Qz – quartz; P – primary; PS – pseudosecondary, S – secondary; Hom – homogeneous; Het – heterogeneous; φ_{vap} – vapor fraction; eq – equivalent; L – liquid; V – vapor; H – halite. PEM – Post-entrapment modification. † For details see Supplementary Material 1; * – samples from the Troodo ophiolite.

and 0.25; Fig. 6D). Salinities are 3.1–3.2 wt.% $NaCl_{eq}$, with T_h(LV→L) of 160–180 °C in one sample and 265–270 °C in another.

In the axial plagiogranite at Wadi Rajmi, miarolitic cavities that are locally epidote-free contain a spilite generation of quartz (coating the early magmatic–hydrothermal quartz) enclosing abundant submicroscopic needles of actinolite and apatite (Fig. S1E). Intergrown with the needles are primary assemblages of aqueous LV inclusions with uniform $\varphi_{vap} \sim 0.3$. Salinities are 2.7–3.0 wt.% $NaCl_{eq}$ and T_h(LV→L) values are 290–313 °C.

In the miarolitic cavities at the Bani Umar North post-axial plagiogranite, spilite-generation quartz encloses crystallites of actinolite and apatite (Fig. 9F1). Located between the mineral inclusions are primary, euhedral, aqueous LV inclusions with uniform $\varphi_{vap} \sim 0.6$ (Fig. 9F2), salinities of 3.7–4.0 wt.% $NaCl_{eq}$ and T_h(LV→L) of 383–390 °C.

Similarly to the Semail plagiogranites, spilite-generation quartz in the miarolitic cavities in the Platanistasa plagiogranite, Troodos, contains swarms of actinolite and chlorite crystallites along growth zones (e.g., sample LR18-Tr06; Fig. S6B). Between these mineral inclusions are primary LV aqueous inclusions with uniform $\varphi_{vap} \sim 0.25$, indicating homogeneous entrapment. The salinity is 5.2 wt.% $NaCl_{eq}$ and T_h(LV→L) varies over a narrow range of 318–323 °C.

5.2.4. Epidosite fluid

In the Semail ophiolite, no primary fluid inclusions were found within epidote, quartz or titanite in the rock matrix of the massive, granoblastic epidosites that pervasively replace former spilitized Geotimes basalts and dikes in the SDC. However, tractable fluid inclusions were found in three other settings: (1) in mm–cm long, freely grown epidote and quartz crystals that line lava drainage cavities within the massive epidosites (Fig. 7A), (2) epidosite-generation quartz (very dark CL) in miarolitic cavities in the plagiogranites (Fig. 9B, C), and (3) in mm–cm wide epidote–quartz veins within the massive replacement epidosites (Figs. 5B, 7B). Euhedral epidotes in these three sample types contain unequivocal primary and pseudosecondary assemblages of fluid inclusions, in which individual inclusions are commonly elongated parallel to the long axis of the host crystals (Fig. 7D). The assemblages consist of aqueous LV inclusions (≤20 μm long) with uniform φ_{vap} of 0.25–0.3, indicating trapping of a homogeneous fluid. Salinities are 3.1–4.0 wt.% $NaCl_{eq}$ and T_h(LV→L) values are 275–370 °C (Table 4), with individual assemblages displaying narrow ranges of up to 10 degrees. In the coexisting euhedral quartz, which shows clear petrographic evidence of being coeval with epidote (e.g., Fig. 7E), fluid inclusion assemblages are present on sets of healed fractures that terminate inside the crystals at former growth zones. The equant, anhedral LV inclusions (≤25 μm diameter) in these pseudosecondary assemblages have constant $\varphi_{vap} \sim 0.2$–0.25 (Fig. 7F). Salinities are 2.6–3.9 wt.% $NaCl_{eq}$ and T_h(LV→L) values are 252–305 °C (Table 4), with individual assemblages exhibiting narrow ranges of less than 15 degrees.

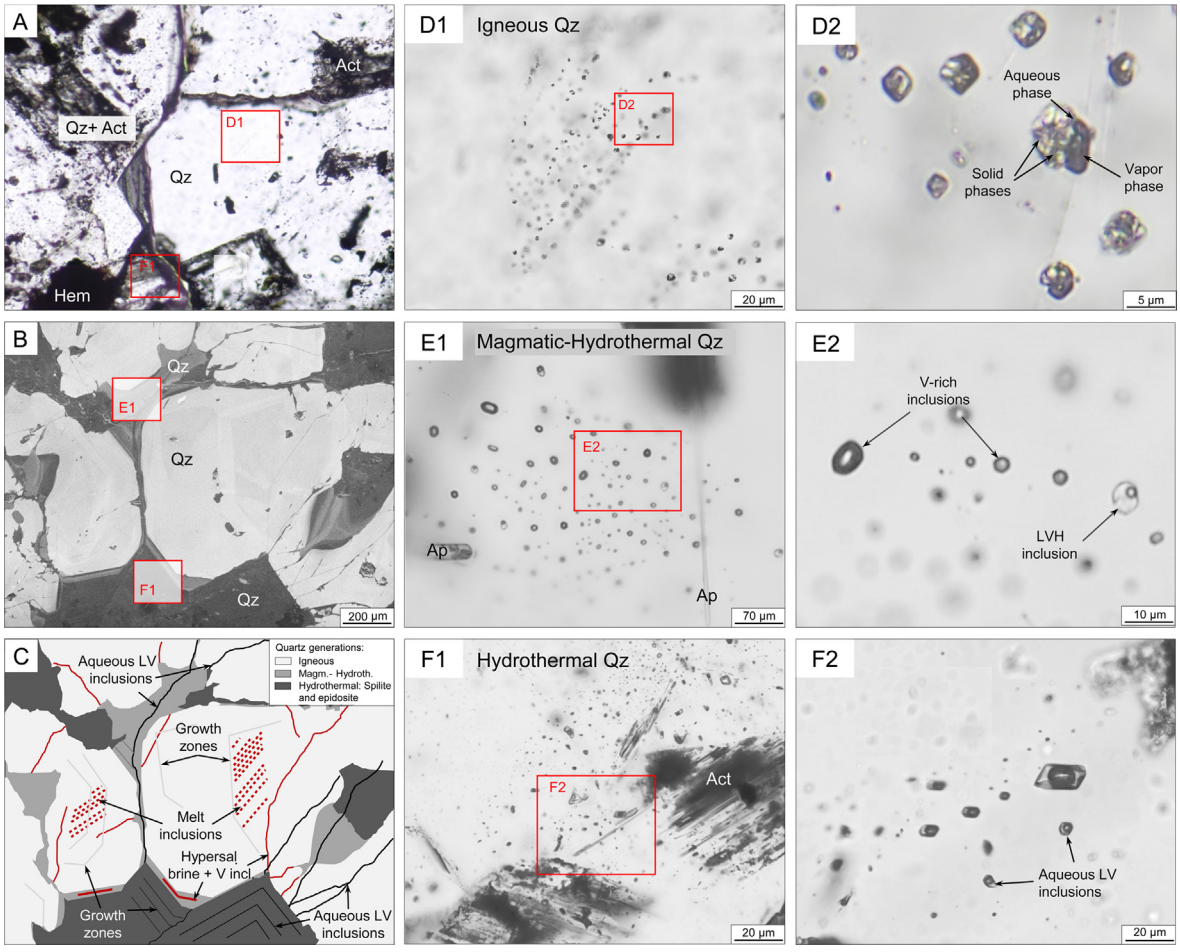

Fig. 9. Microphotographs and relative timing relationships of different Qz generations and their inclusions in the post-axial Bani Umar North plagiogranite, Semail ophiolite (Sample: LR17-BUN-Ta): (A) Transmitted light. (B) SEM-VPSE cathodoluminescence (CL): almost white – igneous Qz with melt inclusions; medium-grey – magmatic–hydrothermal Qz in growth zones and along healed fractures in igneous Qz; dark grey –hydrothermal Qz in latest growth zones and fracture fills. (C) Sketch of image B. (D1, D2) Primary melt inclusions in igneous Qz. (E) Pseudosecondary LVH and coexisting V-dominated LV inclusions along growth zones in magmatic–hydrothermal Qz. (F) Primary LV inclusions in growth zones of hydrothermal Qz coeval with actinolite (microphotograph from an equivalent thick section). Abbreviations: Act – actinolite; H – halite; L – liquid; Qz – quartz; V – vapor.

Outside the massive replacement epidosites in the Semail lavas, vesicles and drainage cavities in the spilitized Geotimes basalts occasionally contain fans of coarse-grained epidote crystals without any accompanying quartz (Fig. 10A, B). These epidotes may represent distal manifestations of the epidotizing fluid that elsewhere formed replacement epidosites. Individual epidote crystals contain primary assemblages of aqueous LV inclusions arrayed along growth zones (Fig. 10C, D). Uniform $\varphi_{vap} \sim 0.25$ indicates homogeneous entrapment. Salinities are 3.1–3.2 wt.% $NaCl_{eq}$ and $T_h(LV \rightarrow L)$ values are 275–280 °C.

In the Semail SDC, no primary fluid inclusions were found in the granoblastic epidote within the massive replacement epidosites (Fig. 5A). However, we found one sample of these epidosites with anhedral quartz that contains LV inclusions with variable φ_{vap} of 0.15–0.8. The quartz displays no growth zones or healed fractures in the CL image, and the inclusions appear to be distributed as three-dimensional clusters within the host crystals. Therefore, the inclusions are deduced to belong to assemblages that are primary in origin. In the liquid-rich inclusions with $\varphi_{vap} \sim 0.15$, salinity is 4.7–5.1 wt.% $NaCl_{eq}$ with $T_h(LV \rightarrow L)$ at 160–210 °C. The inclusions richest in vapor (with $\varphi_{vap} \sim 0.8$) have a salinity of 1.6 wt.% $NaCl_{eq}$. The petrographic relationships are unclear, and in the available assemblages it is not possible to determine whether the variation in φ_{vap} is due to post-entrapment modifications such as necking-down, or whether it represents entrapment of a heterogeneous fluid. The timing of entrapment with respect to epidotization is also unclear: the anhedral quartz that hosts the inclusions could have formed in either the spilitization or epidotization events. Owing to these uncertainties, these inclusions are not considered further in this study.

We were unable to find unequivocal primary fluid inclusions in epidote–quartz veins that cross-cut massive epidosites in the Semail SDC (Fig. 5B). However, one vein contains quartz crystals with secondary inclusions in healed fractures (Fig. 5D), and the quartz is overgrown by much

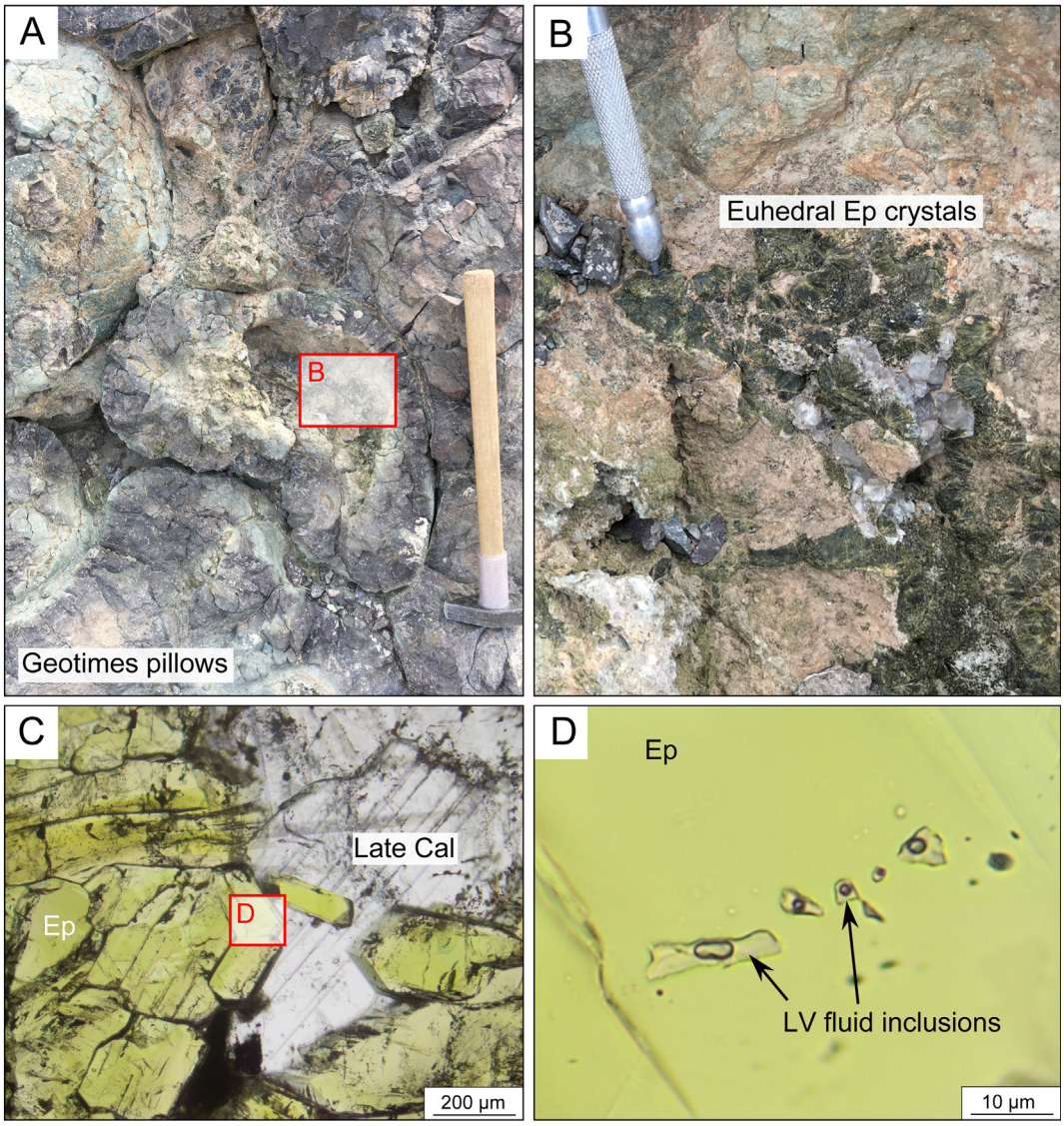

Fig. 10. Field- and micro-photographs of a lava drainage cavity filled with euhedral epidote crystals: (A) Drainage cavity in the center of a spilitized pillow lava filled with (B) euhedral epidote crystals up to 2 cm long. (C, D) Close-ups of euhedral epidote crystals hosting primary LV inclusions. Abbreviations as in Figs. 5 and 6; Cal – calcite.

younger calcite. The quartz-hosted inclusions have euhedral to anhedral shapes and are ≤25 µm in diameter (Fig. 5D). An assemblage of such inclusions (sample LR17-WH-SD-Ep03) shows uniform $\varphi_{vap} \sim 0.2$, salinity of 2.9–3.2 wt.% $NaCl_{eq}$ and T_h(LV→L) at 250–260 °C. These values overlap with those found in primary inclusions in the lava drainage cavities in the massive epidosites. In contrast, the late calcite overgrowths in this sample contains primary inclusions with notably lower salinity and T_h than the quartz-hosted inclusions (see Supplementary Material 1). It is therefore probable that the secondary inclusions in quartz trapped the fluid that formed the epidote–quartz veins.

In notable contrast to the Semail samples, our collection of massive replacement epidosites from the Troodos SDC contains quartz with abundant primary fluid inclusions, distributed as 3D clusters throughout the crystals (Fig. S5). These LV aqueous inclusions have elongated to equant, subhedral to anhedral shapes and the assemblages display uniform $\varphi_{vap} \sim 0.3$, indicating homogeneous entrapment. Submicroscopic crystallites of epidote (confirmed by Raman analysis) are occasionally present within the fluid inclusions. The high variation in $\varphi_{epidote}$ (0–0.1) rules out the origin of these crystallites as daughter crystals and instead indicates that they were trapped simultaneously with the homogeneous aqueous fluid. Salinities are 3.1–3.2 wt.% $NaCl_{eq}$ and T_h(LV→L) values cluster tightly at 272–283 °C.

In the Troodos plagiogranite at Platanistasa, epidote that is intergrown with coeval quartz contains primary assemblages of aqueous LV inclusions with uniform

$\varphi_{vap} \sim 0.2$, indicating homogeneous entrapment. Values of salinity are 3.7–3.9 wt.% $NaCl_{eq}$, with T_h(LV→L) at 358–369 °C.

5.2.5. Fluids in post-epidosite hydrothermal veins in the Semail ophiolite

The post-epidosite prehnite–quartz veins, quartz–hematite ± pyrite veins and calcite veins (Table 1) contain primary or pseudosecondary fluid inclusions that yielded salinities and homogenization temperatures as shown in Fig. 3B and Tables 2 and 4 (details in Supplementary Material 1). The calcite-generation fluids are easily distinguished from the spilite and epidosite fluids, but the salinities and T_h values of the prehnite–quartz and quartz–hematite ± pyrite veins overlap with those of the spilite and epidosite fluids (Fig. 3B). As we characterized the spilite and epidosite fluids exclusively from their primary and pseudosecondary inclusions, this overlap caused no confusion in identification of the fluid generations.

5.3. Chemical compositions of the plagiogranite-, spilite- and epidosite-generation fluids

One of the above-described quartz samples with unequivocal petrographic evidence contains inclusions large enough (~20 μm diameter) for useful LA-ICP-MS analysis. This sample from the Bani Umar North plagiogranite (LR17-BUN-Ta; post-axial plagiogranite intruded the transition of the SDC to Geotimes lavas; Figs. 2 and 8) contains the complete fluid sequence from igneous quartz with melt inclusions, through magmatic–hydrothermal quartz with hypersaline brine and vapor inclusions, spilite quartz hosting LV inclusions and finally epidosite quartz with LV inclusions. Table 5 summarizes the analyses of latter three fluid generations.

To characterize the magmatic–hydrothermal fluid, analyses were made of 57 LVH inclusions and four V-rich inclusions distributed among six fluid inclusion assemblages. Raman analysis showed trace amounts of CO_2 vapor along with H_2O vapor in all the inclusions. For the LVH and V-rich inclusions, LA-ICP-MS analysis yielded ratios of the elements Li, B, Na, Mg, Cl, K, Ca, Fe, Br, Rb, Sr and Ba. In the V-rich inclusions the elements Li, B, Ca, Br and Ba were detected in only one inclusion. The dominant cations in LVH and V-rich inclusions are Na, K and Fe. Full analytical data including limits of detection (LOD) can be found in the Research Data.

To characterize the spilite fluid, two assemblages containing a total of 28 inclusions were analyzed by Raman spectroscopy, again showing traces of CO_2, and by LA-ICP-MS, yielding ratios of all 12 elements. Calculations according to Section 5.3 (Fig. S12) show that the observed range of T_m(Ice) from -2.4 to -1.4 °C corresponds to 2.7–4.4 wt.% TDS.

In the vapor bubbles of the fluid inclusions in the epidosite-generation quartz, H_2O was the only component detected by Raman spectroscopy. Analysis by LA-ICP-MS of 27 LV inclusions in two assemblages yielded ratios of all elements except for Fe (Research Data). Applying the same calculations to the epidosite fluids as for the spilite fluids, the range of salinity is 2.5–4.3 wt.% TDS, essentially identical to that of the spilite fluid.

In the spilite and epidosite fluids, Na and Cl are the most abundant elements followed by Ca, whereas in the hypersaline brines and in the coexisting magmatic–hydrothermal vapors K and Fe exceed Ca. For the epidosite fluid, only a maximum possible concentration of Fe is available, set by the lowest LOD in the analyzed assemblage (7.0×10^{-4} mol/kg_{H2O}). This LOD concentration is far too high for equilibrium with the hematite-bearing epidosite mineral assemblage at the estimated fluid trapping temperature (275–295 °C; Section 5.4). We therefore set the Fe concentration to the fully speciated, thermodynamically calculated equilibrium value at 300 °C (Weber et al., 2021), which is about 4.0×10^{-6} mol/kg_{H2O}.

5.4. *P–T* conditions of fluid inclusion trapping

Since the spilitizing and epidotizing fluids were trapped as single-phase fluids in the Semail inclusions, their homogenization temperatures represent minimum limits on fluid trapping temperatures (T_{trap}; see principles in Diamond, 2003). The true values of T_{trap} and of trapping pressure (P_{trap}) lie somewhere along the *P–T* trajectories of the fluid inclusion isochores (lines of constant density). Fig. 11 shows the range of isochores at the investigated localities calculated from salinity and T_h(LV→L) values (e.g., point 1 in Fig. 11A) using the AqSo_NaCl P–T–V_m–x correlation for the binary H_2O–NaCl system in Bakker (2018; based on Driesner and Heinrich, 2007; Driesner, 2007).

The isochores in Fig. 11 can be used to estimate the pressure of fluid trapping (P_{trap}) by first estimating the depth of trapping below sealevel (i.e., the sum of seawater depth plus paleostratigraphic depth below seafloor) and then adopting a relationship between depth and fluid pressure. We have used the synvolcanic ocean depth of 3.1–3.5 km (corresponding to pressures of 31–35 MPa) defined by the overlap between sedimentary CCD evidence and volatile contents in glass in the paleobathymetric study of the Semail ophiolite by Belgrano et al. (2021). The paleostratigraphic depth of each sample was converted to hydrostatic pressure taking into account the density of the fluid at trapping, as defined by the relevant isochores. Details are provided in Supplementary Material 2.

The maximum and minimum P_{trap} values can be used to determine the temperature of trapping (T_{trap}) and hence the temperature of rock alteration, by intersection with the isochores in Fig. 11. For example, the range in P_{trap} for the spilite fluid at the Rusays locality is 31–54 MPa. In Fig. 11A these bounding pressures (blue P_{trap} lines) intersect isochore 1 at 146 °C (point 2) and at 159 °C (point 3). The small spread in isochores constrains the range of T_{trap} to 25 degrees, i.e., from 146–171 °C, thereby defining a field (green) of possible *P–T* conditions of fluid trapping. In summary, the Semail localities record spilite alteration over a broad, 290 degree range of 146–438 °C at fluid pressures of >31–54 (Fig. 11A), whereas epidosite alteration is recorded at a narrower, 180 degree range of 255–436 °C at fluid pressures of 35–68 MPa (Fig. 11B).

Table 5
Average composition of spilite fluid and epidosite fluid compared to magmatic–hydrothermal hypersaline brine and coexisting vapor from a plagiogranite (this study, sample LR17-BUN-Ta, Bani Umar North) and compared to modern seafloor hydrothermal vent fluid and unmodified seawater.

		Epidosite fluid (27 inclusions, 3.2 wt.% TDS[1])	1 SD	Spilite fluid (28 inclusions, 4.2 wt.% TDS[1])	1 SD	Plagiogranite hypersaline brine (57 inclusions[2], 40.7 wt.% TDS[1])	1 SD	Plagiogranite vapor (4 inclusions[2], 2.9 wt.% TDS[1])	1 SD	Seawater[3] (3.5 wt.% TDS[1])
T	°C	274–294 †		401–438 †		430–300		430–300		0
Li	mol/kg_{H2O}	0.005	0.004	3.1E-4	4.7E-5	0.003	0.003	2.3E-4	–	2.8E-5
B	mol/kg_{H2O}	6.6E-4	2.5E-4	9.3E-4	3.3E-4	0.002	0.001	8.9E-5	–	4.2E-4
Na	mol/kg_{H2O}	0.439	–	0.396	–	4.195	–	0.231	–	0.486
Mg	mol/kg_{H2O}	9.8eE-4	–	0.001	0.001	0.003	0.002	0.008	3.9E−6	0.055
Cl	mol/kg_{H2O}	0.599 *	–	0.727 *	–	8.20	–	0.525 *	–	0.566
K	mol/kg_{H2O}	0.012	0.004	0.056	0.035	1.68	0.305	0.075	0.014	0.011
Ca	mol/kg_{H2O}	0.069	0.021	0.094	0.072	0.245	0.079	0.009	–	0.011
Fe	mol/kg_{H2O}	4.0E-6 (Calc.)	–	0.029	0.023	0.989	0.376	0.082	0.022	3.4E-9
Rb	mol/kg_{H2O}	1.3E-5	7.6E-6	7.6E-5	3.9E-5	0.002	0.001	2.0E-4	1.8E-4	1.3E-6
Sr	mol/kg_{H2O}	1.3E-4	6.0E-5	9.0E-5	4.1E-5	0.001	0.001	4.2E-5	3.6E-5	9.4E-5
Br	mol/kg_{H2O}	0.002	0.001	0.002	0.002	0.032	–	0.004	–	8.7E-4
Ba	mol/kg_{H2O}	4.9E-5	2.1E-5	5.8E-5	3.2E-5	0.034	0.025	4.7E-5	–	1.4E-7
CO_2	mol/kg_{H2O}	n.d.	–	trace	–	trace	–	trace	–	–

[1] Total dissolved solids (not NaCl equivalent); [2] hypersaline liquid in phase-separated LVH inclusions; [3]Na, Mg, Cl, Ca, Sr from Millero et al., (2008); Li, B, Fe and Br from Butterfield et al. (1990); Rb in vent fluid from 13° N East Pacific Rise and in seawater from Palmer and Edmond (1989); Ba from Charlou et al. (1996); † Temperature of fluid trapping estimated from reconstructed hydrostatic pressure (see text for explanation); * calculated from charge balance assuming Cl is the only significant anion; (Calc.) – from Weber et al., 2021; Mg in the vent fluid corresponds to the limit of effective detection owing to contamination by seawater; n.d. – Not detected.

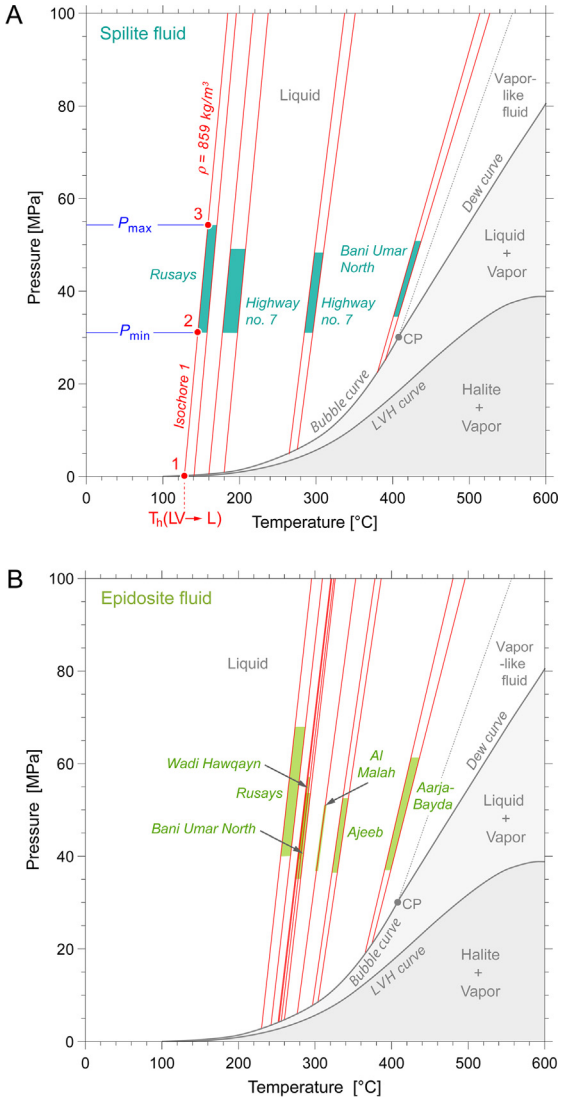

Fig. 11. P–T conditions of spilite and epidosite alteration at the studied locations in the Semail ophiolite, illustrated in the P–T diagram of seawater modelled with 3.2 wt.% $NaCl_{eq}$. Thin lines represent isochores through the liquid field calculated using the correlation of Bakker (2018) for the ranges of T_h and salinities determined by microthermometry at each locality. Fluid P_{min} and P_{max} are calculated as explained in Supplementary Material 2. Intersection of the isochores with P_{min} and P_{max} defines the possible P–T conditions of rock alteration (colored bands) at each site. (A) Spilite alteration. (B) Epidosite alteration.

6. DISCUSSION

6.1. Reliability and representativeness of results

In all our analyzed assemblages of homogeneously trapped fluid inclusions with low salinities (<5.3 wt.% NaCl), the ranges of T_m(Ice) are less than 0.3 degrees and the ranges of T_h are typically less than 20 degrees. This tight grouping of values within individual assemblages supports the conclusion that none of the inclusions selected for analysis has undergone post-entrapment modification. Further, all the fluid inclusions that we have observed, regardless of whether they have been modified after entrapment and hence ignored during analysis, fall into one of the six aqueous fluid generations defined by our petrography (Table 2).

However, only a small number of tractable assemblages of unequivocal primary or pseudosecondary fluid inclusions could be used to characterize the fluid generations. Indeed, none of the Semail massive epidosite samples yielded primary fluid inclusion assemblages in the rock matrix, and so our deductions rely on assemblages in the cogenetic and spatially associated cavity fillings and epidote–quartz veins. Despite having only a limited number of unequivocal fluid inclusion assemblages for analysis in the Semail samples, the fact that we have examined more than 75 petrographic sections lends confidence that our results are representative, as well as pertinent for the alteration processes of interest.

6.2. Origin of the plagiogranite fluids

The miarolitic cavities in the axial and post-axial plagiogranites appear texturally identical, although they are somewhat larger and more abundant in the post-axial stocks. Two field features have important genetic implications: (1) the amphibole-free pegmatitic intergrowths of coarse igneous quartz and plagioclase around the cavities are indicative of enhanced water contents in the most evolved portions of the magma; (2) the myriads of mostly unconnected cavities are regularly distributed throughout large volumes of the plagiogranites. These features attest to the origin of the cavities as pockets of magmatic–hydrothermal fluids that exsolved from the melt during the final stage of plagiogranite crystallization.

6.3. Constraints on the origin of the spilite fluid

6.3.1. Endmember vs. mixed "spilite" fluid in Bani Umar North plagiogranite

The spilite-generation fluid inclusions in the Bani Umar North plagiogranite are clearly later than the hypersaline liquid + low-salinity vapor inclusions in the magmatic–hydrothermal quartz (Section 5.2). Mixing calculations based on the multi-element compositions of the two fluid generations (Supplementary Material 3) rule out the possibility that the analyzed spilite fluid is contaminated by magmatic–hydrothermal hypersaline liquid or low-salinity vapor. This spilite fluid is therefore taken as an example of the fluid that induced widespread spilite alteration in the sheeted dikes and lavas (with allowance for differences in local water–rock ratios and P–T conditions of spilitization subtly modifying its element ratios).

6.3.2. Phase state and origin of salinity in the spilite fluid

Our samples from the Semail ophiolite show that the axial Geotimes lavas and the axial and post-axial plagiogranites were spilitized by circulation of single-phase (liquid) aqueous solutions with salinities of 2.4–5.7 wt.% $NaCl_{eq}$ (Fig. 12), straddling the salinity range of modern seawater (2.8–3.6 wt.% $NaCl_{eq}$). Moreover, the Bani Umar North spilite fluid inclusions have a molar Br/Cl ratio

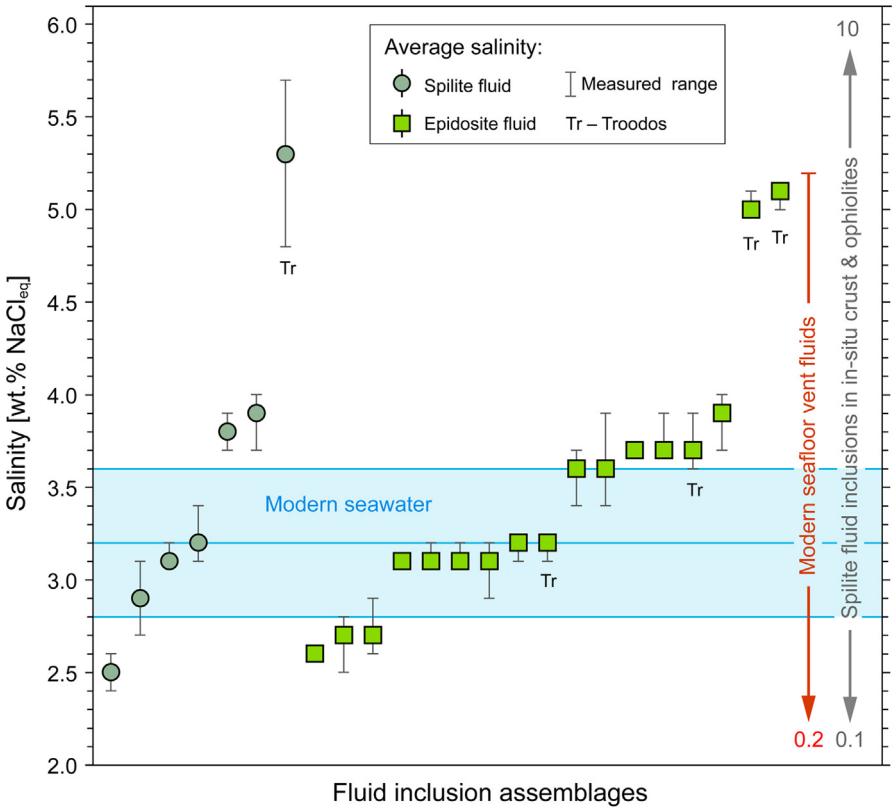

Fig. 12. Salinities of spilite- and epidosite-fluids from the Troodos (labelled Tr) and Semail ophiolites measured in this study. Range bars show the variation of salinity in individual fluid inclusion assemblages. Instrumental uncertainty (±0.18 wt.% $NaCl_{eq}$ = ±0.1 °C) is not shown. Modern seawater after Levitus et al. (1994). Range of modern seafloor vent fluids from Von Damm (2000) and Gallant and Von Damm (2006).

(0.002 ± 0.002 SD) that is compatible within the large analytical uncertainty with the molar Br/Cl ratio of modern seawater (0.0015; Millero et al., 2008; Butterfield et al., 1990). Based on the preservation of this ratio of conservative elements, an origin of the spilite fluid as modified seawater appears certain. In a third of the samples, the salinity is between 3.1 and 3.2 wt.% $NaCl_{eq}$, which we interpret to represent the chlorinity of Cenomanian seawater in the Semail realm. The broader salinity range of the remaining samples (well outside the error of our T_m(Ice) measurements; Fig. 12) is similar to but smaller than that found in spilite fluids elsewhere (Fig. 3A, field 1). Possible causes for this spread have been discussed in the literature and their applicability to our results is examined in the following.

(a) Some researchers have suggested that the salinity of Cretaceous seawater was more variable than that of modern seawater (e.g., Brass et al., 1982; Hay, 2008; Friedrich et al., 2008) but others argue for constant salinities during the Phanerozoic (e.g., Johnson and Goldstein, 1993), hence the issue is unclear. On the other hand, it is implausible that seawater above the Semail crust could have evolved appreciably in salinity during the relatively short, 1 million year duration of volcanic activity and subsequent cooling.

(b) Rock hydration during the hydrothermal alteration has often been suggested as a way that salinity might increase (e.g., Delaney et al., 1987), but in view of the elevated water–rock ratios implied by the spilite alteration, this process is unlikely to have increased the salinity of the fluid measurably.

(c) As far as decreasing the chlorinity is concerned, amphibole with ~30–16000 μg/g Cl (Kendrick, 2019), chlorite with ~20–700 μg/g Cl (Kendrick, 2019) and clay minerals, e.g., celadonite with 140–4000 μg/g Cl (Kendrick, 2019) are the only proven sinks for chloride among the alteration minerals in the crust at depths up to amphibolite-facies conditions. However, owing to the elevated water–rock ratios, their cumulative effect on the fluid salinity is also likely to have been minimal.

(d) Studies of active seafloor vent fluids have revealed a wider range in salinities than we have found in the Semail spilite fluids. In fact, vent fluids almost always have chlorinities higher or lower than seawater (German and Von Damm, 2006), varying from 0.2 to 5.2 wt.% $NaCl_{eq}$ (Von Damm, 2000; Gallant and Von Damm, 2006). This range, and the even wider spread found in spilite fluid inclusions in the in-situ crust (<0.1–10 wt.% $NaCl_{eq}$; Fig. 1A), is widely attributed to sub-seafloor boiling near the venting

sites or to liquid–vapor exsolution (i.e., "phase separation" via brine condensation) and segregation with or without remixing deep in the crust (e.g., Delaney et al., 1987; German and Von Damm, 2006).

The similarity between some of our salinity data and those from vent fluids (Fig. 12) calls for a closer examination of our evidence for fluid inclusion trapping in the single-phase state. Following the standard interpretation of the trapping mechanism of fluid inclusion assemblages (e.g., Diamond, 2003), the absence of vapor-rich inclusions in the spilite-generation assemblages implies merely that liquid was *locally* present alone during fluid inclusion entrapment. In principle, it could be argued that a vapor phase did in fact coexist with the liquid in the spilite rock pores, but that it was not trapped in the hydrothermal quartz owing to its different surface wetting and transport properties. However, quartz is known to readily trap vapor as well as liquid in a wide range of hydrothermal environments (the hypersaline liquid and vapor inclusions in the Semail plagiogranites being a case in point). To our knowledge, the literature on experimental and observable modern environments (e.g., geothermal wells) contains no cases of demonstrated liquid–vapor coexistence in which quartz has systematically trapped liquid but excluded vapor. Since we have examined numerous samples throughout the Semail ophiolite and failed to observe vapor, we conclude that the spilitizing fluid was not in contact with vapor at the time of fluid inclusion entrapment. The liquid–vapor exsolution that occasionally shifted its salinity must have occurred previously along the upflow path at greater depth in the crust.

The changes in salinity of our analyzed spilite fluids can be tracked by reconstructing their possible deep flow paths, based on the known P_{trap}–T_{trap} conditions, the P–T loci of phase boundaries of seawater and the P–T dependency of quartz solubility. Fig. 13 schematically illustrates deep sub-horizontal flow along the base of the Semail SDC near an active magma chamber (not shown). Since entrapment of primary fluid inclusions requires precipitation of new quartz, the disposition of quartz solubility isopleths (Akinfiev and Diamond, 2009) constrains the flow path to intersect the inclusion trapping conditions (green fields) during upflow and cooling. Fig. 13A shows the example of a spilite fluid with seawater chlorinity (3.2 wt.% $NaCl_{eq}$) trapped at the Highway 7 locality. The fluid remains in the liquid state with fixed chlorinity throughout its flow path, becoming trapped in inclusions at point 1.

Drawing on Delaney et al. (1987), a mechanism of generating spilite fluids with the observed range of salinities between 2.5 and 3.9 wt.% $NaCl_{eq}$ via liquid–vapor separation is illustrated in Fig. 13B. Along the indicated horizontal and initial upflow segments, the fluid expands continuously, changing from a dense liquid to a vapor-like state at temperatures above the critical isochore (dotted line). At point 1 (arbitrarily chosen at 53 MPa, 495 °C) the fluid intersects the dew curve (i.e., the segment of the LV curve at $T > T_{critical}$), inducing condensation of small amounts of dense, high-salinity liquid. Decompression within the LV field by just 2 MPa and cooling by 5 °C causes exsolution of 6 vol.% hypersaline liquid (28 wt.% $NaCl_{eq}$), reducing the salinity of the dominant vapor to 2.5 wt.% NaCl (point 2 at 51 MPa, 490 °C). Since the phase boundaries for the coexisting fluids lie very close to the dew curve of seawater, further upflow brings both fluids back into the one-phase field, although presumably the dense liquid lags behind owing to the contrast in transport properties. At point 3 the dominant vapor may mix with residual hypersaline liquid from previous events of liquid–vapor separation, and so attain a higher salinity, e.g. 3.9 wt.% $NaCl_{eq}$, as in the quartz-hosted spilite fluid at Bani Umar North (green field). Continued upflow, constrained in Fig. 13B to follow a path of decreasing quartz solubility, leads to precipitation of quartz and trapping of primary fluid inclusions at point 4. Thereafter the fluid is shown ascending to the seafloor and venting at 31 MPa and 380 °C. A case where the low-salinity "vapor" generated at point 2 in Fig. 13A has not mixed with hypersaline liquid, but simply contracted into the liquid state upon upflow, is given by the spilite-type fluid inclusions with salinity of 2.5 wt.% $NaCl_{eq}$ at Rusays (Fig. 11A).

Although constrained by our observations, much of the flow path in Fig. 13B is arbitrary, notably the cooling between points 2 to 3. Nevertheless, the path appears feasible because it is similar to the dew-curve intersection deduced for fluids in the 4.5 km IDDP-2 borehole into the sheeted dike complex below Iceland (Bali et al., 2020). We see no obstacle to the fluid at point 1 in Fig. 13B having penetrated the LV field under open-system conditions, as segregation of the dense liquid lowers the initial fluid volume by 2 vol.%. Irrespective of the liquid condensation, however, the illustrated upflow path of the "vapor" is characterized by significant volume expansion.

6.3.3. Validity of the spilite fluid composition

As far as we are aware, the multi-element analyses of the spilite and epidosite fluids presented in Section 5.3 are the first obtained on fluid inclusions of near-seawater salinity from oceanic crust. Although measured by state-of-the-art LA-ICPMS, they are relatively imprecise; at least an order or magnitude less precise than typical analyses of seafloor vents. This is due to the technical challenges of analyzing picogram quantities of solutes in such small and weakly saline fluid inclusions. On the other hand, the analyses do not suffer from contamination by cold seawater, as is the case for most sampled vent fluids.

To test the plausibility and broad accuracy of the spilite fluid analyses, two tests can be conducted. The first is a qualitative check that elements depleted in the spilite rocks by seawater–basalt interaction are enriched in the spilite fluid and visa versa, thereby respecting crustal-scale mass-balance constraints (Fig. 14). Relative to the mean composition of four fresh Geotimes–Lasail basalt glasses, the spilitized Geotimes lavas in the Semail ophiolite are depleted in K, Ca, Fe, Rb, Sr and Ba. As expected, the spilite fluid is enriched in these elements relative to seawater. Most notable is the huge enrichment of Fe in the spilite fluid. Sodium and Mg, in contrast, are enriched in the spilite rocks relative to fresh basalt and are accordingly depleted in the spilite fluid relative to seawater. Lithium and B do not appear to follow

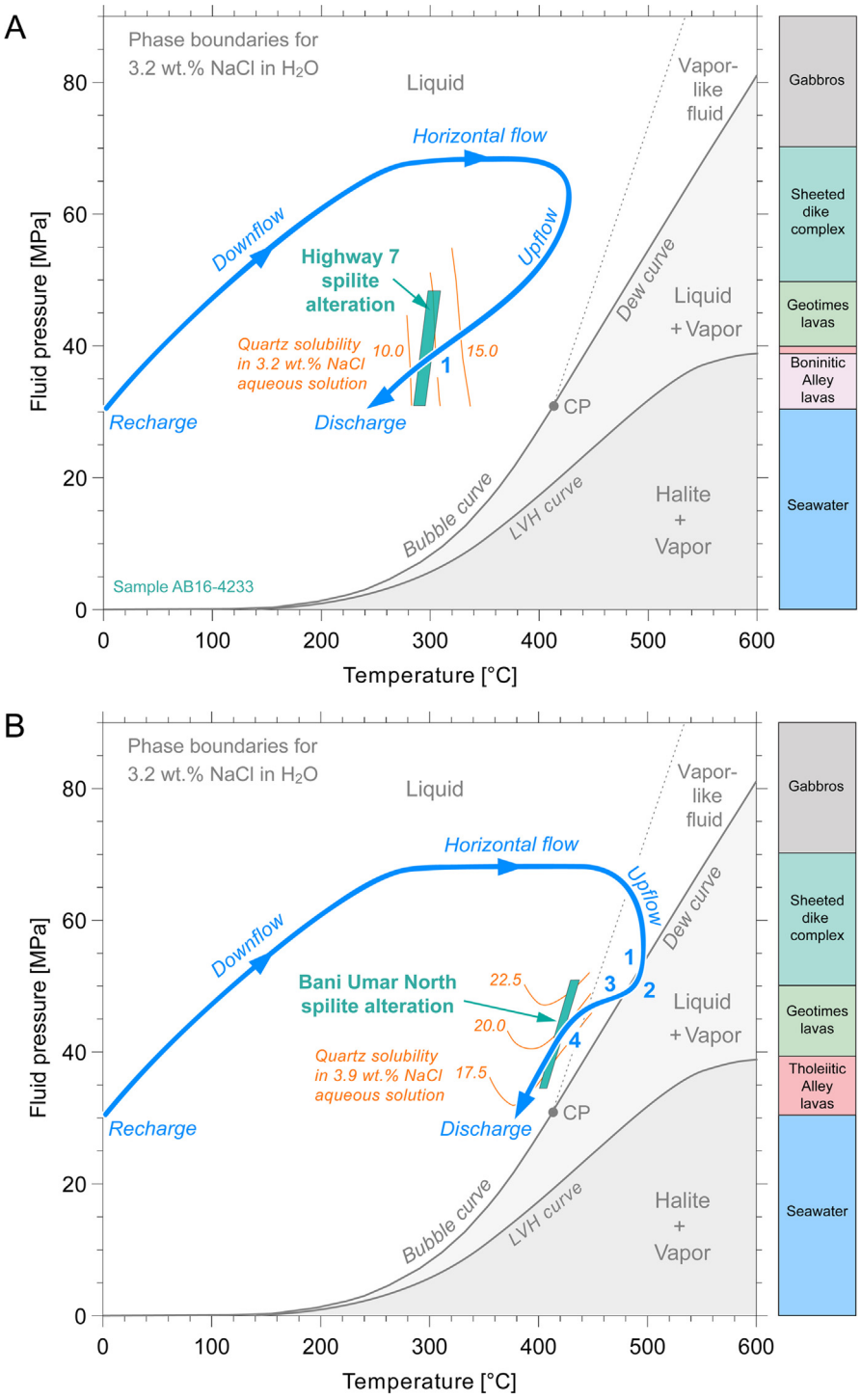

Fig. 13. Schematic *P–T* paths illustrating scenarios of trapping of spilite fluids in the analyzed fluid inclusions. Similar scenarios apply to the epidosite fluids. Stratigraphic columns pertain to the specific localities at the times of trapping. Isopleths of quartz solubility (mmol/kg_{H2O}) calculated from Akinfiev and Diamond (2009) using molar volumes from AqSo_NaCl (Bakker, 2018). (A) Highway 7 locality, sample AB16-4233: fluid with seawater salinity (3.2 wt.% $NaCl_{eq}$) remains in the liquid field and is trapped as primary fluid inclusions in quartz at point 1. (B) Bani Umar North locality, sample LR17-BUN-Ta: liquid initially with seawater salinity expands into a vapor-like fluid along its upflow path and intersects the dew curve at point 1. At point 2 it exsolves minor (6 vol.%) hypersaline liquid with salinity of 28 wt.% $NaCl_{eq}$, shifting the salinity of the remaining vapor to 2.5 wt.% NaCl. Cooling of the two fluids into the one-phase field allows partial mixing at point 3, generating the 3.9 wt.% NaCl fluid trapped as primary fluid inclusions in quartz at point 4.

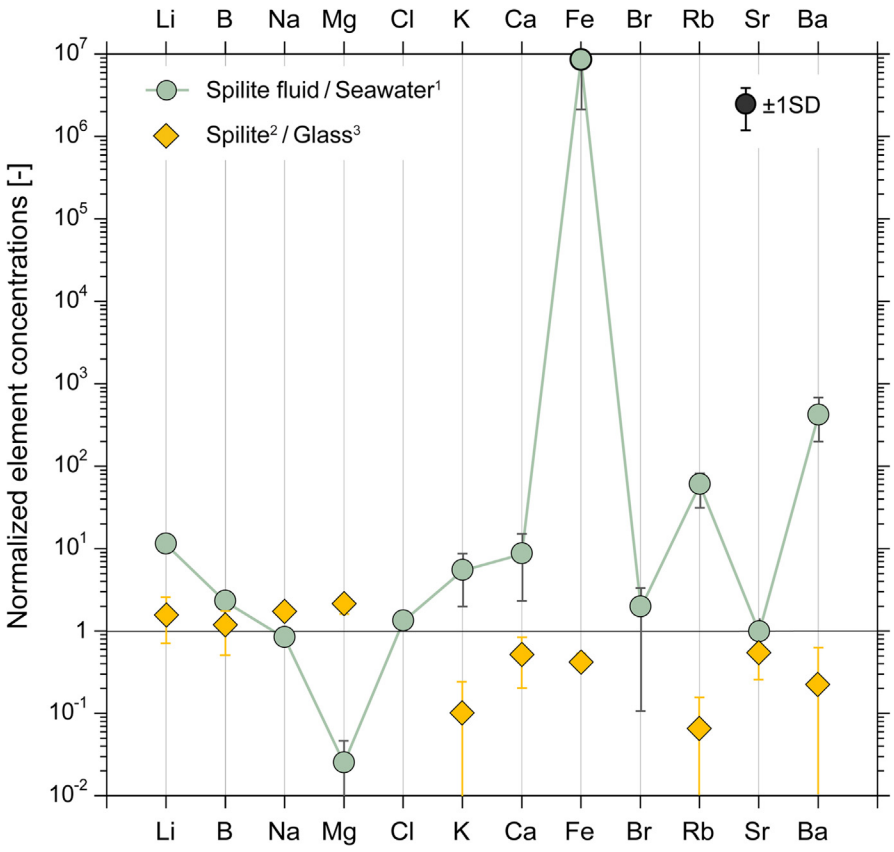

Fig. 14. Enrichment and depletion of elements in spilite fluid (this study) relative to modern seawater[1] (Palmer and Edmond, 1989; Butterfield et al., 1990; Charlou et al., 1996; Millero et al., 2008), and in bulk spilitized Geotimes and Lasail lavas[2] (Belgrano and Diamond, 2019, with Ca corrected for contamination by post-calcite veinlets using 61 own CO_2 analyses) relative to fresh basalt glass[3] (V1 = Geotimes/Lasail basalt, Kusano et al., 2017).

this simple scheme. Apart from the latter exceptions, the composition of the spilite fluid is consistent with the mass-balance constraints, supporting the validity of the analyses.

A second test is a qualitative check on whether the differences in element concentrations between the spilite fluid and seawater match those expected for seawater–basalt interaction up to greenschist-facies conditions (Fig. 15). The extreme depletion of the fluid in Mg conforms to the experimentally verified metasomatic trends of heated seawater reacting with basalt (e.g., Mottl, 1983). In the absence of major mineral sinks for B and Br in the altered basalts, the concentrations of these elements lie close to those of seawater, as expected. Owing to the stabilization of albite in the spilite mineral assemblage in exchange for anorthite component in plagioclase, Na is present at only about 80% of its average molar concentration in seawater. Calcium is enriched relative to Cenomanian seawater, but the average Sr concentration is indistinguishable from that in modern seawater, suggesting that their ratio has been modified by water–rock interaction. Along with Ca, the concentrations of fluid-mobile elements Li, K, Rb and Ba are all highly enriched in the spilite fluid. Iron, the only redox element plotted, is significantly enriched owing to the reduced redox state of the spilite fluid compared to that of seawater. Overall, the fit of the element concentrations with the expectations underscores the validity of the analyses.

6.4. Constraints on the origin of the epidosite fluid

6.4.1. Salinity, phase state and relationship of the epidosite fluid to seawater

All our analyses of epidosite-generation fluids from the Semail and Troodos ophiolites indicate that they were single-phase aqueous liquids at the moment of trapping in fluid inclusions. Their salinities vary from 2.6 to 5.1 wt.% $NaCl_{eq}$, i.e., from values below to above the range of Cenomanian seawater (Fig. 12). Based on the same reasoning as in Section 6.3.2, high-temperature liquid–vapor exsolution at depth below the sampling sites (e.g. Fig. 13B) remains the most plausible explanation for the range in salinities. Again, the implication is that the epidosite fluids were trapped along upflow paths. Nevertheless, numerous fluid inclusion samples in Fig. 12 cluster at 3.1–3.2 wt.% $NaCl_{eq}$. This value could well represent the chlorinity (~560 mmol/kg Cl) of Cenomanian seawater that had not undergone any liquid–vapor exsolution during the hydrothermal alteration in the Semail and Troodos ophiolites (e.g. Fig. 13A).

Our salinity and T_h measurements agree with the subset of previous studies that attribute epidosite formation to seawater-like fluids, as summarized in Fig. 3B and Section 3.2 (Richardson et al., 1987; Nehlig and Juteau, 1988; Schiffman and Smith, 1988) but they contradict the second subset that attribute formation of massive replace-

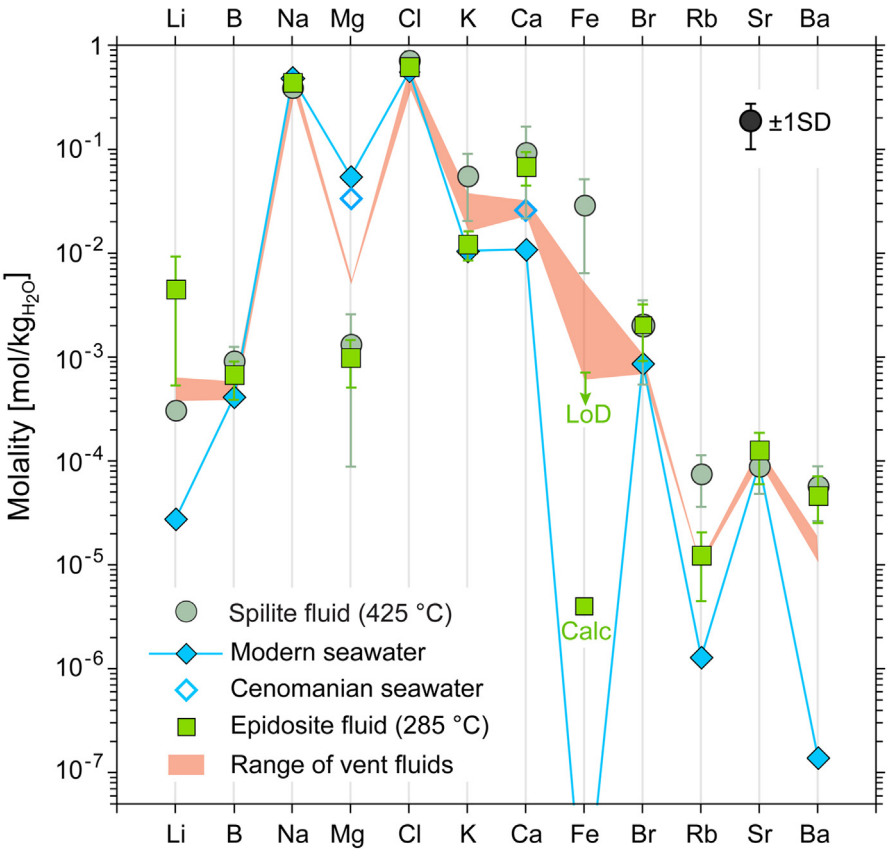

Fig. 15. Element concentrations (molality) in spilite fluid at 425 °C (this study) and epidosite fluid at 285 °C (this study) compared to modern seawater (Palmer and Edmond, 1989; Butterfield et al., 1990; Charlou et al., 1996; Millero et al., 2008), Cenomanian seawater (Timofeeff et al., 2006) and modern seafloor vent fluids (range of vent fluids: Juan de Fuca, Butterfield et al., 1990; Scotia Ridge vents, James et al., 2014; TAG, Schmidt et al., 2017 and references therein). LoD: Limit of detection. Calc: Thermodynamically calculated concentration of Fe from Weber et al. (2021), see text.

ment epidosites to hypersaline brines (Cowan and Cann, 1988; Juteau et al., 2000). In agreement with the observations of Kelley et al. (1992) in Troodos, we have found that hypersaline brines are spatially and temporally restricted to plagiogranites in both the Semail and Troodos ophiolites and that the brines in fact exsolved from the plagiogranite melts. The contradicted studies of Cowan and Cann (1988) and Juteau et al. (2000) drew their evidence for hypersaline brines from epidotized plagiogranites in Troodos and Semail, respectively. In contrast to the findings in the massive epidosites, Kelley et al. (1992) found hypersaline and coexisting vapor inclusions in cm-size epidote pods in the Troodos plagiogranites and suggested that the epidote formed by deuteric alteration. We do not rule out this suggestion, although we have not found such inclusions in the epidote + quartz assemblages in our Troodos samples. However, our CL imaging has shown that the hypersaline brines are older than and genetically unrelated to the overprinting massive epidosites. Furthermore, spilite alteration systematically occurs in the time interval *between* magmatic fluid exsolution and late epidosite alteration in the plagiogranites of both ophiolites. Since the zonation of the quartz in the plagiogranites is complex and extremely difficult to discern under the normal petrographic microscope, we suspect that the lack of CL imaging in the earlier, contradicted studies led to misleading petrographic observations. Thus, all our fluid inclusion evidence speaks against the formation of large massive replacement epidosites by magmatic–hydrothermal hypersaline fluids. However, recent REE and Sr-isotope studies (Anenburg et al., 2015; Fox et al., 2020) argue that plagiogranite fluids play the prime role in forming massive epidosites in both the plagiogranites and the surrounding SDC. Further work is required to reconcile the two types of evidence.

6.4.2. Chemical composition of the epidosite fluid

Fig. 15 and Table 5 show the elemental composition of the reconstructed epidosite fluid trapped at 275–295 °C at Bani Umar North, which has the unmodified salinity of Cenomanian seawater. The pattern of element concentrations in Fig. 15 is in many respects similar to that of the spilite fluid, hence we consider the LA-ICP-MS analyses to be just as valid as those of the spilite fluid (Section 6.3.3). As epidosites in Oman are known to replace precursor spilites (Section 2.3), one way to view the epidosite fluid is as an evolved form of an earlier spilite fluid that was chemically modified by fluid–rock interaction (but not necessarily by liquid–vapor exsolution), such that Na and Mg can be

quantitatively leached and replaced by Ca (e.g., Weber et al., 2021). However, the Ca/Mg and Ca/Na ratios in the analyzed epidosite and spilite fluids are not significantly different given the available precision. Potassium and Rb appear to be lower in the epidosite fluid, perhaps because these elements had already been depleted in the spilite precursors. However, the most obvious difference between the two fluids is the concentration of Fe. The very low calculated content in the epidosite fluid (4.0×10^{-6} mol/kg$_{H2O}$) is consistent with all Fe in the epidosite alteration being oxidized and therefore insoluble. Finally, the conservative elements B and Br (and Cl) appear similar, as expected from the lack of mineral sinks for these elements.

6.4.3. Relationship of spilite and epidosite fluids to vent fluids on the modern basaltic seafloor

The spilite and epidosite fluids are compared to modern basalt-hosted, black-smoker seafloor vent fluids in Fig. 15. Mean values of the East Scotia Ridge vent (James et al., 2014), Juan de Fuca (Butterfield et al., 1990) and TAG (Schmidt et al., 2017 and references therein) have been chosen for this comparison because they include a large number of analyzed elements. The spilite fluid matches several features of the vent fluids (contents of Li, B, Na, Cl, K, Br and Sr), but Ca, Fe (and possibly Rb and Ba) are higher in the spilite fluid. The elevated Ca and Fe concentrations may reflect the fact that these elements (and Ba) tend to precipitate as sulfates and sulfides just below or at the seafloor, such that typical vent-sampling methods do not capture the higher concentrations present in the deeper upflowing fluid. Magnesium in the spilite fluid is notably lower than in the plotted mean vent fluid (Mg value from East Scotia Ridge vents), but this may be due to the difficulties of determining Mg concentration in the pristine venting fluids, owing to contamination by cold seawater (German and Von Damm, 2006). Based on these comparisons, it seems plausible that the analyzed spilite fluid at 425 °C could have acted as a feeder fluid to a typical basalt-hosted, black-smoker vent.

The comments made above regarding B, Mg, Br, Rb and Sr in the spilite fluid compared to the vent fluids also apply to the epidosite fluid. However, as emphasized by Weber et al. (2021), the estimated concentration of Fe in the epidosite fluid is incompatible with black-smoker type fluids. Although the epidosite fluids represent upflowing hydrothermal solutions, they appear to be too poor in Fe to form pyrite-rich VMS deposits at or just below the seafloor. We are unaware of an other type of seafloor vent fluid that could match our analyzed epidosite fluid. While their elevated Ca content suggests that the epidosite fluids would generate sulphate chimneys upon focused venting into normal sulphate-rich seawater, it is also possible that they vent diffusely without noticeable seafloor precipitates and have therefore not been recognized so far.

7. SUMMARY AND CONCLUSIONS

We have conducted a field, petrographic and analytical study on fluid inclusions petrographically attributable to spilite-type (chlorite + albite + quartz ± actinolite ± epidote) and epidosite-type (epidote + quartz + titanite + hematite or magnetite) hydrothermal alteration in the basaltic upper crust of the Semail ophiolite, with supporting samples from the Troodos ophiolite. The sampled geological settings in the Semail ophiolite include the sheeted dike complex, the comagmatic (axial) Geotimes lavas, and axial and post-axial plagiogranite stocks in the sheeted dikes and Geotimes lavas.

All our samples consistently show that the spilite and epidosite alteration was caused by single-phase (homogeneous) aqueous liquids. However, their salinities vary between sampling sites. In a third of the samples, the salinity is between 3.1 and 3.2 wt.% $NaCl_{eq}$, which we interpret to represent the chlorinity of Cenomanian seawater in the Semail realm. The remaining samples have salinities as low as 2.4 wt.% $NaCl_{eq}$ and as high as 5.7 wt.% $NaCl_{eq}$. This spread can be quantitatively explained by modest degrees of liquid–vapor separation and remixing that occurred deeper in the crust prior to the fluids being trapped as single-phase liquids at the sampling sites. The implication is that samples with salinities lower or higher than Cenomanian seawater were formed along upflow segments of the fluid paths, consistent with previous studies of spilite-related fluid inclusions in in-situ crust and in the Semail and Troodos ophiolites.

Similarly, our results regarding the phase state and salinity of the epidosite fluid agree with several previous studies on the Semail and Troodos ophiolites, whereas other studies have argued that hypersaline brines formed the massive replacement epidosite bodies. According to our sampling in the two ophiolites, hypersaline brines, often accompanied by vapor, occur only in plagiogranites (both axial and post-axial). These magmatic–hydrothermal fluids exsolved from the plagiogranite melts during final crystallization. Our CL imaging of plagiogranite samples from both ophiolites revealed that the magmatic–hydrothermal fluids predate and are genetically unrelated to the younger spilite fluid and even younger epidosite fluid.

Consideration of the Semail volcanostratigraphy constrains the examined sites to maximum depths between 1470 m and 3600 m below seafloor at the time of fluid inclusion trapping. Taking account of paleo-ocean depths between 3100 and 3500 m, the spilite fluids were trapped at 145–440 °C and >31–54 MPa and the epidosite fluids at 255–435 °C and 35–68 MPa.

The precision of our elemental analyses of the spilite and epidosite fluids is well below that of typical vent fluid analyses, but they nevertheless yield valid and useful results. The Br/Cl ratio of the spilite fluid matches that of modern seawater, and the concentrations of most of the other analyzed elements in the spilite fluid match those of modern basalt-hosted black-smoker vents, including very low Mg. The exceptions are elements that typically precipitate just below or at the seafloor, prior to sampling of vent fluids, namely Ca and Fe. These are enriched in the spilite fluid compared to the vent fluids. Accordingly, the composition of the spilite fluid fits qualitatively well with known chemical trends associated with the chemical reequilibration of seawater as it moves through hot basaltic crust. Moreover, the analyzed spilite fluid, which

induced albite–quartz–actinolite alteration at temperatures of 400–440 °C, could well have discharged at a typical black-smoker vent.

The epidosite fluid appears to be a derivative of the spilite fluid that underwent stronger chemical modification by water–rock interaction, including oxidation. Whereas most elements in the epidosite fluid are also compatible with black-smoker venting, the extremely low Fe content of the epidosite fluid argues against a direct link. Although the high Ca and Ba contents could perhaps generate sulfate chimneys upon discharge, the epidosite fluid seems incapable of forming Fe-sulfide deposits at the seafloor.

Our *P*–*T*–composition characterizations of the spilite and epidosite fluids are best viewed as snapshots of specific thermodynamic states at specific times, locations and *P*–*T* conditions during the hydrothermal evolution of the Semail and Troodos crust. Given the open-system nature of the fluid–rock interaction, the reconstructed chemical compositions presumably reflect steady-state rather than full equilibrium conditions. As such, these snapshots fill important gaps in the knowledge of fluids in the deep realms of the volcanic and sheeted dike sequences, beyond the current capabilities of sampling by seafloor drilling. They also provide calibration targets for future numerical simulations of reactive transport through the oceanic crust.

Declaration of Competing Interest

The authors declare that they have no known competing financial interests or personal relationships that could have appeared to influence the work reported in this paper.

ACKNOWLEDGEMENTS

We thank Thomas Belgrano, Alannah Brett and Samuel Weber for field assistance and discussions, and Thomas Monecke for comments on an early version of the manuscript. Help with analyses was provided by Thomas Pettke for LA-ICP-MS. We gratefully acknowledge the logistical support of Khalid al-Tobi (Earth Secrets Co., Oman) and the Ministry of Energy and Minerals, Sultanate of Oman. Comments by journal reviewers Clifford Patten, Andrew McCaig and an anonymous expert helped clarify this article. This project was funded by Swiss National Science Foundation (SNSF) Grant 200020-169653 to L.W. Diamond.

RESEARCH DATA

Research data associated with this article has been submitted with this manuscript.

SUPPLEMENTARY MATERIAL

Supplementary data to this article can be found online at https://doi.org/10.1016/j.gca.2021.11.012.

REFERENCES

Adamides N. G. (2010) Mafic-dominated volcanogenic sulphide deposits in the Troodos ophiolite, Cyprus Part 2-A review of genetic models and guides for exploration. *Appl. Earth Sci.* **119**, 193–204.

Akinfiev N. N. and Diamond L. W. (2009) A simple predictive model of quartz solubility in water–salt–CO_2 systems at temperatures up to 1000 °C and pressures up to 1000 MPa. *Geochim. Cosmochim. Acta* **73**, 1597–1608.

Alabaster T., Pearce J. A. and Malpas J. (1982) The volcanic stratigraphy and petrogenesis of the Oman ophiolite complex. *Contrib. Miner. Petrol.* **81**, 168–183.

Alabaster T. and Pearce J. A. (1985) The interrelationship between magmatic and ore-forming hydrothermal processes in the Oman ophiolite. *Econ. Geol.* **80**, 1–16.

Alt J. C., Laverne C., Coggon R. M., Teagle D. A. H., Banerjee N. R., Morgan S., Smith-Duque C. E., Harris M. and Galli L. (2010) Subsurface structure of a submarine hydrothermal system in ocean crust formed at the East Pacific Rise, ODP/IODP Site 1256. *Geochem. Geophys. Geosyst.* **11**, Q10010.

Anenburg M., Katzir Y., Rhede D., Jöns N. and Bach W. (2015) Rare earth element evolution and migration in plagiogranites: a record preserved in epidote and allanite of the Troodos ophiolite. *Contrib. Miner. Petrol.* **169**.

Bakker R. J. (2018) AqSo_NaCl: Computer program to calculate p-T-V-x properties in the H_2O-NaCl fluid system applied to fluid inclusion research and pore fluid calculation. *Comput. Geosci.* **115**, 122–133.

Bakker R. J. and Diamond L. W. (2006) Estimation of volume fractions of liquid and vapor phases in fluid inclusions, and definition of inclusion shapes. *American Mineralogist* **91**(4), 635–657.

Bali E., Aradi L. E., Zierenberg R., Diamond L. W., Pettke T., Szabó A., Guðfinnsson G. H., Friðleifsson G. O. and Szabó C. (2020) Geothermal energy and ore-forming potential of 600 °C mid-ocean-ridge hydrothermal fluids. *Geology* **48**, 1221–1225.

Banerjee N. R., Gillis K. M. and Muehlenbachs K. (2000) Discovery of epidosites in a modern oceanic setting, the Tonga forearc. *Geology* **28**, 151–154.

Belgrano T. M. and Diamond L. W. (2019) Subduction-zone contributions to axial volcanism in the Oman–U.A.E. ophiolite. *Lithosphere* **11**, 399–411.

Belgrano T. M., Diamond L. W., Vogt Y., Biedermann A. R., Gilgen S. A. and Al-Tobi K. (2019) A revised map of volcanic units in the Oman ophiolite: insights into the architecture of an oceanic proto-arc volcanic sequence. *Solid Earth* **10**, 1181–1217.

Belgrano T. M., Tollan P. M., Marxer F. and Diamond L. W. (2021) Paleobathymetry of Submarine Lavas in the Samail and Troodos Ophiolites: Insights From Volatiles in Glasses and Implications for Hydrothermal Systems. *J. Geophys. Res. Solid Earth* **126**, e2021JB021966.

Bettison-Varga L., Schiffman P. and Janecky D. R. (1995) Fluid-rock interaction in the hydrothermal upflow zone of the Solea graben, Troodos ophiolite, Cyprus. In *Low-grade metamorphism of mafic rocks*, vol. 296 (eds. P. Schiffman and H. W. Dey). Geol. Soc. Am. Spec. Pap., pp. 81–100.

Brass G. W., Southam J. R. and Peterson W. H. (1982) Warm saline bottom waters in the ancient ocean. *Nature* **296**, 620–623.

Butterfield D. A., Massoth G. J., McDuff R. E., Lupton J. E. and Lilley M. D. (1990) Geochemistry of hydrothermal fluids from Axial Seamount Hydrothermal Emissions Study vent field, Juan de Fuca Ridge. *J. Geophys. Res.* **95**, 12895–12921.

Cann J. (1969) Spilites from the Carlsberg Ridge, Indian Ocean. *J. Petrol.* **10**, 1–19.

Cann J. R., McCaig A. M. and Yardley B. W. D. (2015) Rapid generation of reaction permeability in the roots of black smoker systems, Troodos ophiolite, Cyprus. *Geofluids* **15**, 179–192.

Castelain T., McCaig A. M. and Cliff R. A. (2014) Fluid evolution in an Oceanic Core Complex: A fluid inclusion study from IODP Hole U1309 D—Atlantis Massif, 30°N, Mid-Atlantic Ridge. *Geochem. Geophys. Geosyst.* **15**, 1193–1214.

Charlou J. L., Fouquet Y., Donval J. P., Auzende J. M., Jean-Baptiste P., Stievenard M. and Michel S. (1996) Mineral and gas chemistry of hydrothermal fluids on an ultrafast spreading ridge: East Pacific Rise, 17° to 19°S (Naudur cruise, 1993) phase separation processes controlled by volcanic and tectonic activity. *J. Geophys. Res.* **101**, 15899–15919.

Coogan L. A. (2008) Reconciling temperatures of metamorphism, fluid fluxes, and heat transport in the upper crust at intermediate to fast spreading mid-ocean ridges. *Geochem. Geophys. Geosyst.* **9**, Q02013.

Cowan J. and Cann J. (1988) Supercritical two-phase separation of hydrothermal fluids in the Troodos ophiolite. *Nature* **333**, 259–261.

Delaney J. R., Mogk D. W. and Mottl M. (1987) Quartz-cemented breccias from the Mid-Atlantic Ridge: Samples of a high-salinity hydrothermal upflow zone. *J. Geophys. Res.* **92**(B9), 9175–9192.

Diamond L. W. (1990) Fluid inclusion evidence for P-V–T–X evolution of hydrothermal solutions in late-alpine gold-quartz veins at Brusson, Val d'Ayas, northwest Italian Alps. *Amer. J. Sci.* **290**, 912–958.

Diamond L. W. (2003) Systematics of H_2O inclusions. In *Fluid Inclusions: Analysis and Interpretation*, vol. 32 (eds. I. M. Samson, A. J. Anderson and D. D. Marshall). Min. Ass. Canada Short Course, pp. 55–79.

Driesner T. and Heinrich C. A. (2007) The System H_2O–NaCl. I. Correlation Formulae for Phase Relations in Temperature-Pressure-Composition Space from 0 to 1000 °C, 0 to 5000 bar, and 0 to 1 X_{NaCl}. *Geochim. Cosmochim. Acta* **71**, 4880–4901.

Driesner T. (2007) The System H_2O-NaCl. II. Correlations for molar volume, enthalpy, and isobaric heat capacity from 0 to 1000 °C, 1 to 5000 bar, and 0 to 1 X_{NaCl}. *Geochim. Cosmochim. Acta* **71**, 4902–4919.

Fox S., Katzir Y., Bach W., Schlicht L. and Glessner J. (2020) Magmatic volatiles episodically flush oceanic hydrothermal systems as recorded by zoned epidote. *Commun. Earth Environ.* **1**, 52.

Friedrich O., Erbacher J., Moriya K., Wildon P. A. and Kuhnert H. (2008) Warm saline intermediate waters in the Cretaceous tropical Atlantic Ocean. *Nat. Geosci.* **1**, 453–457.

Fusswinkel T., Giehl C., Beermann O., Fredriksson J. R., Garbe-Schönberg D., Scholten L. and Wagner T. (2018) Combined LA-ICP-MS microanalysis of iodine, bromine and chlorine in fluid inclusions. *J. Anal. At. Spectrom.* **33**, 768–783.

Gallant R. M. and Von Damm K. L. (2006) Geochemical controls on hydrothermal fluids from the Kairei and Edmond Vent Fields, 23°–25°S, Central Indian Ridge. *Geochem. Geophys. Geosys.* **7**, Q06018.

Galley A. G. (1993) Characteristics of semi-conformable alteration zones associated with volcanogenic massive sulphide districts. *J. Geochem. Explor.* **48**, 175–200.

Gallinatti B. C. (1984) Initiation and collapse of active circulation in a hydrothermal system at the Mid-Atlantic Ridge, 23°N. *J. Geophys. Res.* **89**, 3275–3289.

Gass I. G. (1980) The Troodos Massif; its role in the unravelling of the ophiolite problem and its significance in the understanding of constructive plate margin processes. In *Ophiolites. Proceedings, International ophiolite symposium. Nicosia, Cyprus* (ed. A. Panayiotou), pp. 23–35.

German C. R. and Von Damm K. L. (2006) Hydrothermal processes. In *Treatise on Geochemistry 6. The oceans and marine geochemistry* (eds. H. D. Holland, K. K. Turekian and H. Elderfield). Elsevier-Pergamon, Oxford, UK, pp. 181–222.

Gilgen S. A., Diamond L. W., Mercolli I., Al-Tobi K., Maidment D. W., Close R. and Al-Towaya A. (2014) Volcanostratigraphic Controls on the Occurrence of Massive Sulfide Deposits in the Semail Ophiolite, Oman. *Econ. Geol.* **109**, 1585–1610.

Gilgen S. A., Diamond L. W. and Mercolli I. (2016) Sub-seafloor epidosite alteration: timing, depth and stratigraphic distribution in the Semail ophiolite, Oman. *Lithos* **260**, 191–210.

Gillis K. M. (2002) The Rootzone of an Ancient Hydrothermal System Exposed in the Troodos Ophiolite, Cyprus. *J. Geol.* **110**, 57–74.

Gillis K. M. and Robinson P. T. (1990) Patterns and processes of alteration in the lavas and dykes of the Troodos Ophiolite, Cyprus. *J. Geophys. Res.* **95**, 21523–21548.

Gillis K. M. and Banerjee N. R. (2000) Hydrothermal alteration patterns in supra-subduction zone ophiolites. In *Ophiolites and Oceanic Crust: New Insight from Field Studies and the Ocean Drilling Program*, vol. 349 (eds. Y. Dilek, E. M. Moores, D. Elthon and A. Nicolas). Geol. Soc. Am. Spec. Pap., pp. 283–297.

Götte T., Pettke T., Ramseyer K., Koch-Müller M. and Mullis J. (2011) Cathodoluminescence properties and trace element signature of hydrothermal quartz: a fingerprint of growth dynamics. *Amer. Miner.* **96**, 802–813.

Guillong M., Meier D. L., Allan M. M., Heinrich C. A. and Yardley B. W. D. (2008) SILLS: A MATLAB-based program for the reduction of laser ablation ICP–MS data of homogeneous materials and inclusions. In *Laser ablation ICP-MS in the Earth Sciences: Current practices and outstanding issues*, vol. 40 (eds. H. Longerich and P. Sylvester). Min. Ass. Canada Short Course, pp. 328–333.

Haase K. M., Freund S., Beier C., Koepke J., Erdmann M. and Hauff F. (2016) Constraints on the magmatic evolution of the oceanic crust from plagiogranite intrusions in the Oman ophiolite. *Contrib. Minal. Petrol.* **171**, 1–16.

Harper G. D. (1995) Pumpellyosite and prehnitite associated with epidosite in the Josephine ophiolite—Ca metasomatism during upwelling of hydrothermal fluids at a spreading axis. *Geol. Soc. of Am. Spec. Pap.* **296**, 101–122.

Hay W. W. (2008) Evolving ideas about the Cretaceous climate and ocean circulation. *Cretac. Res.* **29**, 725–753.

Heft K. L., Gillis K. M., Pollock M. A., Karson J. A. and Klein E. M. (2008) Role of upwelling hydrothermal fluids in the development of alteration patterns at fast spreading ridges: Evidence from the sheeted dike complex at Pito Deep. *Geochem. Geophys. Geosyst.* **9**, Q05O07.

Hannington M. D., Santaguida F., Kjarsgaard I. M. and Cathles L. M. (2003) Regional-scale hydrothermal alteration in the Central Blake River Group, western Abitibi subprovince, Canada: implications for VMS prospectivity. *Miner. Depos.* **38**, 393–422.

Hannington M. (2014) Volcanogenic Massive Sulfide Deposits. In *Treatise on Geochemistry 2nd Ed. 13* (eds. H. D. Holland and K. K. Turekian). Elsevier, Oxford, UK, pp. 463–488.

James R. H., Green D. R. H., Stock M. J., Alker B. J., Banerjee N. R., Cole C., German C. R., Huvenne V. A. I., Powell A. M. and Connelly D. P. (2014) Composition of hydrothermal fluids and mineralogy of associated chimney material on the East Scotia Ridge back-arc spreading centre. *Geochim. Cosmochim. Acta* **139**, 47–71.

Jochum K. P., Wilson S. A., Abouchami W., Amini M., Chmeleff J., Eisenhauer A., Hegner E., Iaccheri L. M., Kieffer B., Krause J., McDonough W. F., Mertz-Kraus R., Raczek I., Rudnick R.

L., Scholz D., Steinhoefel D., Stoll B., Stracke A., Tonarini S., Weis D., Weis U. and Woodhead J. D. (2011) GSD-1G and MPI-DING reference glasses for in situ and bulk isotopic determination. *Geostandards and Geoanalytical Research* **35**, 193–226.

Johnson W. J. and Goldstein R. H. (1993) Cambrian seawater preserved as inclusions in marine low-magnesium calcite cement. *Nature* **362**, 335–337.

Jowitt S. M., Jenkin G. R. T., Coogan L. A. and Naden J. (2012) Quantifying the release of base metals from source rocks for volcanogenic massive sulphide deposits: effects of protolith composition and alteration mineralogy. *J. Geochem. Explor.* **118**, 47–59.

Juteau T., Manach G., Moreau O., Lecuyer C. and Ramboz C. (2000) The high temperature reaction zone of the Oman ophiolite: new field data, microthermometry of fluid inclusions, PIXE analyses and oxygen isotopic ratios. *Mar. Geophys. Res.* **21**, 351–385.

Kelley D. S. and Robinson P. T. (1990) Development of a brine-dominated hydrothermal system at temperatures of 400–500°C in the upper level plutonic sequence. *Geochim. Cosmochim. Acta* **54**, 653–661.

Kelley D. S., Robinson P. T. and Malpas J. G. (1992) Processes of brine generation and circulation in the oceanic crust: fluid inclusion evidence from the Troodos ophiolite, Cyprus. *J. Geophys. Res.* **97**(B6), 9307–9322.

Kelley D. S. and Früh-Green G. L. (2001) Volatile lines of descent in submarine plutonic environments: Insights from stable isotope and fluid inclusion analyses. *Geochim. Cosmochim. Acta* **65**, 3325–3346.

Kendrick M. A. (2019) Halogens in altered ocean crust from the East Pacific Rise (ODP/IODP Hole 1256D). *Geochim. Cosmochim. Acta* **261**, 93–112.

Kusano Y., Umino S., Shinjo R., Ikei A., Adachi Y., Miyashita S. and Arai S. (2017) Contribution of slab-derived fluid and sedimentary melt in the incipient arc magmas with development of the paleo-arc in the Oman Ophiolite. *Chem. Geol.* **449**, 206–225.

Lambrecht G. and Diamond L. W. (2014) Morphological ripening of fluid inclusions and coupled zone-refining in quartz crystals revealed by cathodoluminescence imaging: implications for CL-petrography, fluid inclusion analysis and trace-element geothermometry. *Geochim. Cosmochim. Acta* **141**, 381–406.

Landtwing M. R. and Pettke T. (2005) Relationships between SEM-cathodoluminescence response and trace-element composition of hydrothermal vein quartz. *Am. Mineral.* **90**, 122–131.

Lecumberri-Sanchez P., Steele-MacInnis M. and Bodnar R. J. (2015) Synthetic fluid inclusions XIX. Experimental determination of the vapor-saturated liquidus of the system H_2O–NaCl–$FeCl_2$. *Geochim. Cosmochim. Acta* **148**, 34–49.

Levitus S., Burgett R. and Boyer T. P. (1994) World Ocean Atlas 1994, vol. 3. Salinity. National Environmental Satellite, Data, and Information Service, Washington, DC (United States).

Lippard S. J., Shelton A. W. and Gass I. G. (1986) The ophiolite of northern Oman. The Geological Society Memoir, vol. 11. Blackwell Scientific Publications, Oxford.

Marien C. S., Hoffmann J. E., Garbe-Schönberg C. D. and Münker C. (2019) Petrogenesis of plagiogranites from the Troodos Ophiolite Complex, Cyprus. *Contributions to Mineralogy and Petrology* **174**, 35.

Millero F. J., Feistel R., Wright D. G. and McDougall T. J. (2008) The composition of standard seawater and the definition of the Reference-Composition Salinity Scale. Deep Sea Res. Part I. *Oceanogr. Res. Pap.* **55**, 50–72.

Miyashita S., Adachi Y. and Umino S. (2003) Along-axis magmatic system in the northern Oman ophiolite: Implications of compositional variation of the sheeted dike complex. *Geochem. Geophys. Geostat.* **4**, 8617.

Mottl M. J. (1983) Metabasalts, axial hot springs, and the structure of hydrothermal systems at mid-ocean ridges. *Geol. Soc. Am. Bull.* **94**, 161–180.

Nehlig P. (1989) Etude d'un systeme hydrothermal oceanique fossile: L'ophiolite de Samail (Oman) Ph.D. thesis. Univ. Bretagne Occidentale, Brest, France.

Nehlig P. (1991) Salinity of oceanic hydrothermal fluids: a fluid inclusion study. *Earth Planet. Sci. Lett.* **102**, 310–325.

Nehlig P. (1994) Fracture and permeability analysis in magma-hydrothermal transition zones in the Samail ophiolite (Oman). *Journal of Geophysical Research* **99**(B1), 589–601.

Nehlig P. and Juteau T. (1988) Flow porosities, permeabilities and preliminary data on fluid inclusions and fossil thermal gradients in the crustal sequence of the Sumail ophiolite, Oman. *Tectonophysics* **151**, 199–221.

Nehlig P., Juteau T., Bendel V. and Cotton J. (1994) The root zones of oceanic hydrothermal systems: constraints from the Semail ophiolite (Oman). *J. Geophys. Res.* **99**, 4703–4713.

Palmer M. R. and Edmond J. M. (1989) The strontium isotope budget of the modern ocean. *Earth Planet. Sci. Lett.* **92**, 11–26.

Patten C. G. C., Pitcairn I. K. and Teagle D. A. H. (2017) Hydrothermal mobilisation of Au and other metals in supra-subduction oceanic crust: Insights from the Troodos ophiolite. *Ore Geol. Rev.* **86**, 487–508.

Pearce J. A., Alabaster T., Shelton A. W. and Searle M. P. (1981) The Oman ophiolite as a Cretaceous arc-basin complex: Evidence and implications. *Philos. Trans. Royal Soc. A* **300**, 299–317.

Pearce J. A. and Robinson P. T. (2010) The Troodos ophiolitic complex probably formed in a subduction initiation, slab edge setting. *Gondwana Res.* **18**(1), 60–81.

Pettke T., Oberli F., Audetat A., Guillong M., Simon A. C., Hanley J. J. and Klemm L. M. (2012) Recent developments in element concentration and isotope ratio analysis of individual fluid inclusions by laser ablation single and multiple collector ICP-MS. *Ore Geol. Rev.* **44**, 10–38.

Pflumio C. (1991) Evidences for Polyphased Oceanic Alteration of the Extrusive Sequence of the Semail Ophiolite from the Salahi Block (Northern Oman). In *Ophiolite Genesis and Evolution of the Oceanic Lithosphere* (eds. T. Peters, A. Nicolas and R. Coleman). Springer, Dordrecht, pp. 313–351.

Quon S. H. and Ehlers E. G. (1963) Rocks of the northern part of the Mid-Atlantic Ridge. *Geol. Soc. Am. Bull.* **74**, 1–8.

Richardson C. J., Cann J. R., Richards H. G. and Cowan J. G. (1987) Metal-depleted root zones of the Troodos ore-forming hydrothermal systems, Cyprus. *Earth Plan. Sci. Lett.* **84**, 243–253.

Rioux M., Benoit M., Amri I., Ceuleneer G., Garber J. M., Searle M. and Leal K. (2021) The origin of felsic intrusions within the mantle section of the Samail ophiolite: Geochemical evidence for three distinct mixing and fractionation trends. *J. Geophys. Res. Solid Earth* **126**, e2020JB020760.

Robinson P. T., Melson W. G., O'Hearn T. and Schmincke H.-U. (1983) Volcanic glass compositions of the Troodos ophiolite, Cyprus. *Geology* **11**, 400–404.

Roedder E. (1981) Origin of fluid inclusions and changes that occur after trapping. In *Fluid inclusions: applications to petrology*, vol. 6 (eds. L. S. Hollister and M. L. Crawford). Mineralogical Association of Canada, Short course, pp. 101–137.

Roedder E. (1984) Fluid Inclusions. *Rev. Mineral. Min. Soc. Am.* **12**.

Saccocia P. J. and Gillis K. M. (1995) Hydrothermal upflow zones in the oceanic crust. *Earth Planet. Sci. Lett.* **136**, 1–16.

Schiffman P. and Smith B. M. (1988) Petrology and oxygen isotope geochemistry of a fossil seawater hydrothermal system within the Solea Graben northern Troodos ophiolite, Cyprus. *J. Geophsy. Res.* **93**, 4612–4624.

Schmidt K., Garbe-Schönberg D., Hannington M., Anderson M., Bühring B., Haase K., Haruel C., Lupton J. and Koschinsky A. (2017) Boiling vapour type fluids from the Nifonea vent field, New Hebrides Island Arc, Vanuatu, SW Pacific: Geochemistry of an early-stage hydrothermal system. *Geochim. Cosmochim. Acta* **207**, 185–209.

Searle M. and Cox J. (1999) Tectonic setting, origin, and obduction of the Oman ophiolite. *Bull. Geol. Soc. Am.* **111**, 104–122.

Seo J. H., Guillong M., Aerts M., Zajacz Z. and Heinrich C. A. (2011) Microanalysis of S, Cl, and Br in fluid inclusions by LA–ICP-MS. *Chem. Geol.* **284**, 35–44.

Staudigel H. (2014) Chemical Fluxes from Hydrothermal Alteration of the Oceanic Crust. In *Treatise on Geochemistry* (eds. H. D. Holland and K. K. Turekian). Elsevier, Oxford, pp. 583–606, second ed..

Steele-Maclnnis M., Bodnar R. J. and Naden J. (2011) Numerical model to determine the composition of H_2O–NaCl–$CaCl_2$ fluid inclusions based on microthermometric and microanalytical data. *Geochim. Cosmochim. Acta* **75**(1), 21–40.

Teagle D. A. H., Alt J. C., Umino S., Miyashita S., Banerjee N. R., Wilson D. S., Coggon R. and Expedition 309/312 Scientists (2006) An intact section of ocean crust formed at a superfast spreading rate. *Proceedings of the Integrated Ocean Drilling Program, 309/312*.

Timofeeff M. N., Lowenstein T. K., Da Silva M. A. M. and Harris N. B. (2006) Secular variation in the major-ion chemistry of seawater: Evidence from fluid inclusions in Cretaceous halites. *Geochim. Cosmochim. Acta* **70**, 1977–1994.

Vanko D. A., Bodnar R. J. and Sterner S. M. (1988) Synthetic fluid inclusions: VIII. Vapor-saturated halite solubility in part of the system NaCl-$CaCl_2$-H_2O, with application to fluid inclusions from oceanic hydrothermal systems. *Geochimica et Cosmochimica Acta* **52**(10), 2451–2456.

Vanko D. A., Griffith J. D. and Erickson C. L. (1992) Calcium-rich brines and other hydrothermal fluids in fluid inclusions from plutonic rocks, Oceanographer Transform, Mid-Atlantic Ridge. *Geochimica et Cosmochimica Acta* **56**(1), 35–47.

Varga R. J., Gee J. S., Bettison-Varga L., Anderson R. S. and Johnson C. L. (1999) Early establishment of seafloor hydrothermal systems during structural extension: paleomagnetic evidence from the Troodos ophiolite Cyprus. *Earth Planet. Sci. Lett.* **171**, 221–235.

Von Damm K. L. (2000) Chemistry of hydrothermal vent fluids from 9°–10°N, East Pacific Rise: "Time zero", the immediate posteruptive period. *Journal of Geophysical Research* **105**(B5), 11203–11222.

Weber S., Diamond L. W., Alt-Epping P. and Brett-Adams A. C. (2021) Reaction Mechanism and Water/Rock Ratios Involved in Epidosite Alteration of the Oceanic Crust. *J. Geophsy. Res. Solid Earth* **126**.

Associate editor: Frieder Klein